ELASTIC ADHESIVE BANDAGE WITH ADJUSTABLE MECHANICAL AND LOW-SWELLING PROPERTIES AS WEARABLE BIOELECTRONICS

MO YONGYI

MPhil

The Hong Kong Polytechnic University

2026

The Hong Kong Polytechnic University

Department of Applied Biology and Chemical Technology

Elastic Adhesive Bandage with Adjustable Mechanical and Low-swelling Properties as Wearable Bioelectronics

Mo Yongyi

A thesis submitted in partial fulfilment of the requirements for the degree of Master of Philosophy

January 2026

Certificate of Originality

I hereby declare that this thesis is my own work and that, to the best of my knowledge and belief, it reproduces no material previously published or written, nor material that has been accepted for the award of any other degree or diploma, except where due acknowledgement has been made in the text.

(Signed)

MO Yongyi

(Name of student)

Abstract

Skin adhesive bandages have drawn great attention as alternatives to conventional clinical closure techniques for healing and sealing damaged or injured wounds. However, current skin adhesives often exhibit compromised therapeutic efficacy due to excessive swelling, mismatched mechanical properties, and poor tissue adhesion. In addition to their traditional application in skin closure, adhesive bandages have been integrated into flexible electronic devices for accurate monitoring of human physiological signals. The secure attachment of flexible and wearable electronic devices requires a soft, elastic and adhesive substrate, thereby facilitating prompt, precise and accurate detection of physiological signals. Unfortunately, most modern adhesive bandage materials rely on van der Waals forces for adhesion, which can be easily disrupted by skin impurities, limiting their effectiveness for long-term and repeated usage. Therefore, the development of novel adhesive bandages is both critical and challenging, aiming to achieve strong and reliable tissue bonding for skin wound sealing as well as enhancing the accuracy and consistency of signal.

In this study, we propose a soft, elastic, and adhesive bandage, which adhered firmly to skin tissue surfaces and exhibited excellent anti-swelling properties, for tight, fit-to-shape skin sealing and secure fixation of flexible electronic devices. The adhesive bandage, termed PLD-PS, was fabricated via a simple, one-step reaction by mixing the poly(lactide-co-propylene glycol) dimethacrylate (P_7L_2DMA, where 7 and 2 denote the unit lengths of polypropylene glycol (PPG) and lactide (LA), respectively), poly(lactide-co-propylene glycol) (P_7L_2) and a four-arm thiol pentaerythritol tetra(3-mercaptopropionate) (PTM) at room temperature. The photocrosslinkable and rigid P_7L_2DMA served as the structural framework, providing mechanical support and enabling a gentle fabrication process suitable for physiological environments. PTM, containing four thiol functional groups per molecule, reacted with the carbon-carbon double bonds (C=C) of P_7L_2DMA via a thiol-ene click reaction during

photocrosslinking, and formed robust adhesion to tissues through disulfide (S-S) bond formation. P_7L_2 primarily modulated the mechanical properties of the adhesive by increasing inter-chain friction and energy dissipation through hydrogen bonds. The PLD-PS was further functionalized by programmable patterning with liquid metal gallium-indium eutectic, enabling the creation of a PLD-PS-based sensor, capable of accurately detecting electrocardiogram (ECG) signals both *in vivo* and *in vitro*.

In this project, we first synthesized P_7L_2 and P_7L_2DMA, then optimized the concentrations of P_7L_2 and PTM (from 0 to 40 wt%) of the PLD-PS. Subsequently, we conducted a comprehensive evaluation of the mechanical, adhesive, swelling, *in vitro* sensing properties, and *in vitro* biocompatibility of PLD-PS. Mechanical properties were assessed by measuring the tensile modulus (ranged from 0.200 ± 0.073 MPa to 9.637 ± 0.260 MPa) and compressive modulus (ranged from 0.753 ± 0.084 MPa to 6.920 ± 0.740 MPa), demonstrating the compatibility of PLD-PS with various soft and hard tissues. The PLD-PS exhibited stable adhesive strength (approximately 60 kPa) and outstanding burst pressure (~1500 mmHg), ensuring conformal adhesion to skin. Furthermore, the PLD-PS displayed minimal swelling (~2% over 5 days) and limited degradation (less than 15% over 21 days), supporting its long-term stability. Additionally, we assessed the *in vitro* cytocompatibility of the PLD-PS with over 95% of cells maintaining viability and sustained proliferation after three days of co-incubation. What's more, PLD-PS demonstrated excellent hemocompatibility, with a hemolysis ratio of less than 1%. At last, the sensing properties of PLD-PS were further assessed, showing a broad sensing range from 0 to over 100% strain. After technological advancements, we fabricated a sandwich-structured PLD-PS-based sensor, encapsulating liquid metal within its middle layer. The newly formed sensor produced stable and reproducible electronic signals, enabling the monitoring of body joint movements (including wrist, elbow, and finger) and the transmission of Morse codes (such as "SOS" and "HELLO"). We envision that our proposed adhesive PLD-

PS bandage exhibits the potential to facilitate rapid and accurate monitoring of ECG signals. Moreover, we anticipate that the PLD-PS adhesive bandage will inspire further research in the development of advanced substrates for flexible electronic devices.

List of Publications

Journal Papers

1. Xu TP, Rao JD, **Mo YY**, Lam A, Wong S, Wong K, Zhao X. 3D printing in musculoskeletal interface engineering: current progress and future directions. Advanced Drug Delivery Reviews, 2025, 219, 115552.
2. Rao JD, Suo D, Ma FQ, **Mo YY**, Bei HP, Wang L, Tang CY Y, Yiu K-H, Wang SQ, Yang ZL*, Zhao X*, Riding a vascular time train to spatiotemporally attenuate thrombosis and restenosis by double presentation of therapeutic gas and biomacromolecules. Exploration, 2025, 5(2): 70004.
3. Rao JD, Mou XH, **Mo YY**, Bei H-P, Wang L, Tang CY Y, Yiu K-H, Yang ZL, Zhao X, Gas station in blood vessels: An endothelium mimicking, self-sustainable nitric oxide fueling stent coating for prevention of thrombosis and restenosis. Biomaterials, 2023, 302, 122311.

Acknowledgements

Firstly, I would like to express my sincere and deepest gratitude to my supervisor, Professor Xin Zhao, for her profound expertise, rigorous scholarship, and approachable demeanour, which have guided me throughout my entire MPhil study. Throughout every stage of my research journey, from research topic selection to experimental guidance and manuscript revision, Prof. Zhao provided meticulous instruction and tireless support. She never gave up on me, even during the moments of limited diligence or understanding; instead, she patiently and earnestly reminded me of the dedication and perseverance required in scientific research. She never blamed me for experimental failures. On the contrary, she worked alongside me to analyse the causes and seek solutions. Whenever new experimental conditions were needed, she supported me without hesitation and was always generous in providing necessary reagents and equipment. The successful completion of my research project is, to a large extent, attributable to Professor Zhao's unwavering support. I am sincerely grateful for her exemplary mentorship and selfless guidance. Having the opportunity to learn from her has been the greatest fortune of my academic career.

Additionally, I am truly grateful to my colleagues and friends at PolyU, for their collaboration and support, including Dr Yuhe Yang, Dr Dawang Zhao, Dr Quanjing Mei, Dr Tianpeng Xu, Dr Shang Lyu, Dr Jingdong Rao, Dr Di Suo, Mr Huaqian Liu, Mr Ho Pan Bei, Mr Ho Yin Andy Yuen, Mr Qi Liu, Miss Xintong Zhou, Mr Xinyang Wang, Mr Zhuowen Hao, and Mr Shuai Zhao, in Prof. Zhao's group, for their consistent support, help, and collaboration. Their constructive suggestions and valuable assistance helped me a lot during my research. It has been a great honour to work in such a team. In particular, I would like to express my deep thankful to Dr. Jingdong Rao for teaching me basic laboratory operations, to Dr Di Suo for helping me throughout the entire project, to Mr. Huaqian Liu for teaching me material synthesis, and to Mr. Qi Liu for helping with circuit printing, as well as for their companionship and encouragement

throughout my research journey.

Furthermore, I am deeply appreciative of the support provided by the technical personnel in the Department of Applied Biology and Chemical Technology, as well as those working in the university's research facilities, whose valuable assistance greatly contributed to my studies at PolyU.

Finally, I wish to sincerely thank my family and boyfriend for their steadfast support, constant encouragement, and boundless affection, which were invaluable throughout my life. The daily care enabled me to devote myself wholeheartedly to my research without reservation. Equally, when I felt weary and disheartened, their support gave me the strength to persevere. I am also grateful to my ordinary, clumsy yet determined self who strives to pursue dreams. May I continue to grow even more passionate in my future PhD studies.

Table of Contents

List of Abbreviations

BCI	Blood clotting index
C=C	Carbon-carbon double bonds
DCM	Dichloromethane
ddH_2O	Distillation-distillation water
DMEM	Dulbecco's modified eagle medium
ECG	Electrocardiography
Ga-In	Gallium-indium eutectic
GelMA	Gelatin methacryloyl
GPS	Global positioning system
HEMA	2-hydroxyethyl methacrylate
^{1}H-NMR	^{1}H-nuclear magnetic resonance
L929	NCTC colon 929 cell
LA	Lactide
MAC	Methacryloylchloride
N_2	Nitrogen
NHS ester	N-hydroxysuccinimides ester
PBS	Phosphate buffered saline
PDMS	Polydimethylsiloxane
PLD-P	P_7L_2DMA-P_7L_2
PLD-PS	P_7L_2DMA-P_7L_2-PTM

PLD-S	P_7L_2DMA-PTM
PPG	Polypropylene glycol
PTM	Tetra(3-mercaptopropionate)
RBC	Red blood cell
TEA	Triethylamine
TMSPMA	3-(trimethoxysilyl)propyl methacrylate
UTM	Universal testing machine
UV	Ultraviolet
WCA	Water contact angle

1. Introduction

With an ageing population and a growing emphasis on healthier lifestyles, the demand for portable, wearable and implantable bioelectronic devices capable of real-time vital sign monitoring has become increasingly important [1, 2]. The current global market for wearable devices, which are normally smartwatches, has experienced rapid growth and technological advancement, with leading brands such as Apple, Samsung, Huawei, and Garmin driving innovation and shaping consumer preferences, reaching a total of approximately 534.6 million products sold globally in 2024 [3]. Modern products offer a comprehensive suite of features, including heart rate and blood oxygen monitoring, ECG, sleep and stress tracking, and global positioning system (GPS), reflecting a growing consumer emphasis on health and convenience [4]. However, the accuracy of these wearable and implantable devices is highly compromised by the insufficient and non-conformal interfacial adhesion between the device and the target site, primarily due to mismatched mechanical properties [5].

Over the last decades, progress in materials science has led to the development of flexible devices with low modulus resembling human skin, to replace traditional rigid devices and maintain better contact for accurate human physiological monitoring in disease diagnosis and treatment. Nevertheless, it appears that these flexible devices tend to lose their interfacial adhesion with the human body due to metabolic by-products secreted by tissues [6]. To ensure long-term stability and fixation, conventional suturing and gluing strategies have been commonly used, whereas, risks of severe drawbacks such as tissue penetration, inflammation, and damage to surrounding tissues are reported [5]. These limitations underscore the urgent need for novel strategies to achieve reliable fixation of flexible wearable and implantable bioelectronic devices. To address these challenges, adhesive bandages are increasingly used as noninvasive alternatives, forming an adhesive layer that promotes functional adhesion between the tissues and flexible devices. Nevertheless, conventional adhesive bandages typically

rely on van der Waals forces for adhesion, which can be compromised by impurities from the skin, limiting their effectiveness for long-term and repeated use. Therefore, the development of novel multifunctional adhesive bandages is both critical and challenging to ensure strong and reliable bonding to tissues. This, in turn, enhances the precision and reliability of signal transmission at the interfaces between sensors and biological tissues.

In addition to their application for adhesive fixation, multifunctional adhesive bandages have also been utilized for skin wound sealing, owing to their conformally fixing and adhering properties. With the advancement of modern surgical techniques, the surgical procedures conducted worldwide annually has surpassed 300 million [7]. Since ancient times, starting from the use of ant jaws, people have explored various methods for skin wound closure. Nowadays, conventional invasive techniques such as suturing, wiring, and stapling are widely utilized in clinical practice as the standard approach [8]. However, concerns about postoperative complications such as incomplete closure, bleeding, and inflammation were reported [9], with statistics showing that postoperative complications were observed in 31.50% of cases, including 8% of patients with major complications and 3.75% with postoperative mortality [10]. To address these limitations, some commercial adhesives are widely chosen for substitution of those traditional skin wound closure techniques in clinical treatment [11], such as glues, hydrogels and polymers, demonstrating advantages of noninvasive, convenient, and biocompatibility [12, 13]. Nevertheless, they still face notable shortcomings, including weak tissue adhesion, poor mechanical properties [14], risk of inflammation [15], and uncontrollable degradation [16], which weaken the applications of these adhesives. Therefore, all of these limitations remain a great challenge and urgent demand to develop novel multifunctional skin wound adhesives integrating good adhesive, mechanical, and sensing properties, as well as biocompatibility.

1.1 Wound adhesives and bandages developed for wound closure and sensing therapy

The complexity of both *in vivo* and *in vitro* environments leads to diverse requirements for skin tissue adhesives and bandages. Ideal products should have robust tissue adhesion to ensure firm, conformal, and long-term attachment, thereby preventing treatment failure and enhancing sensing accuracy [17, 18]. Additionally, tuneable mechanical properties are of great importance to accommodate the varying characteristics of different organs and tissues [19, 20]. Furthermore, a limited swelling ratio is needed, as excessive swelling in the wet environment can compromise both adhesive and mechanical properties [21, 22], resulting in material failure and sensor artefacts. Despite the wide range of potential uses in tissue repair and biomedical device integration, most commercially available adhesives do not fully satisfy these clinical demands. The extensive possibilities in this field remain a focal point for ongoing clinical and scientific research. Here, we summarize current material optimization strategies related to adhesive, mechanical, and swelling properties, and further propose the design approach adopted in this study.

1.1.1 Adhesive properties and mechanisms

With the rapid advancement of materials science, tissue adhesives have emerged as indispensable tools in modern medicine, offering viable substitutes for conventional methods in wound closure and tissue engineering [23]. The effectiveness of these adhesives is fundamentally determined by their adhesion mechanisms, which generally depend on physical, chemical, and structural factors [24] (**Figure 1-1**).

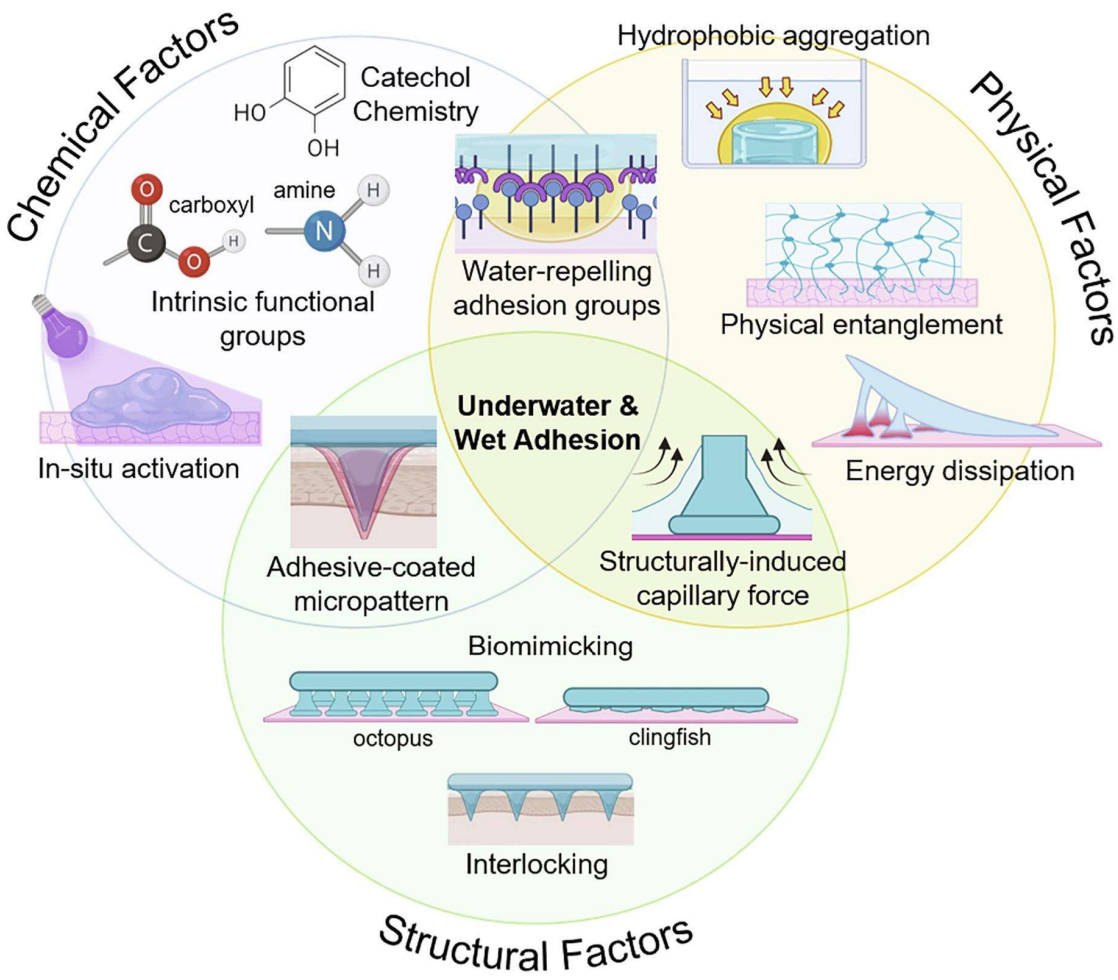

Figure 1-1. Adhesive mechanisms for tissue adhesive materials, including physical, chemical and structural factors. Reproduced with permission from [24], copyright 2022, Elsevier.

Physical adhesion occurs through various non-covalent interactions, including hydrophobic effects, electrostatic forces, π–π interactions, van der Waals interactions, and hydrogen bonds (**Figure 1-2**), enabling rapid and reversible adhesion [25]. For instance, van der Waals forces, though individually weak, become significant when large surface areas are involved. Hydrogen bonding, which can form between polar groups on the adhesive and tissue surfaces, is the most widely adopted physical adhesion strategy in tissue adhesives [26]. The primary advantage of physical adhesion is its rapid onset and reversibility, which is beneficial for applications requiring

temporary fixation or repeated bonding. However, physical adhesion strength decreases quickly in wet or dynamic environments, which are typical of physiological conditions [27].

Chemical adhesion depends on covalent linkages between the adhesive material and tissue surfaces, facilitated by a variety of functional groups, such as NHS esters, mussel-inspired catechols, thiols, and aldehydes [23, 28] (**Figure 1-2**). This mechanism provides stronger and more durable adhesion compared to physical interactions. Wu et al. reported a 3D-printed adhesive that formed tight, wet adhesion to tissues by forming amide bonds via NHS ester groups [7]. What's more, Tian et al. fabricated an adhesive hydrogel containing thiol groups, which can undergo disulfide exchange reactions and form disulfide bonds with thiol groups on tissue surfaces [29]. This adhesive hydrogel demonstrated long-lasting and robust tissue adhesion [22]. These covalent interactions ensure robust and long-lasting adhesion, even in moist or bleeding conditions, making them particularly advantageous for clinical applications where strong tissue integration is required.

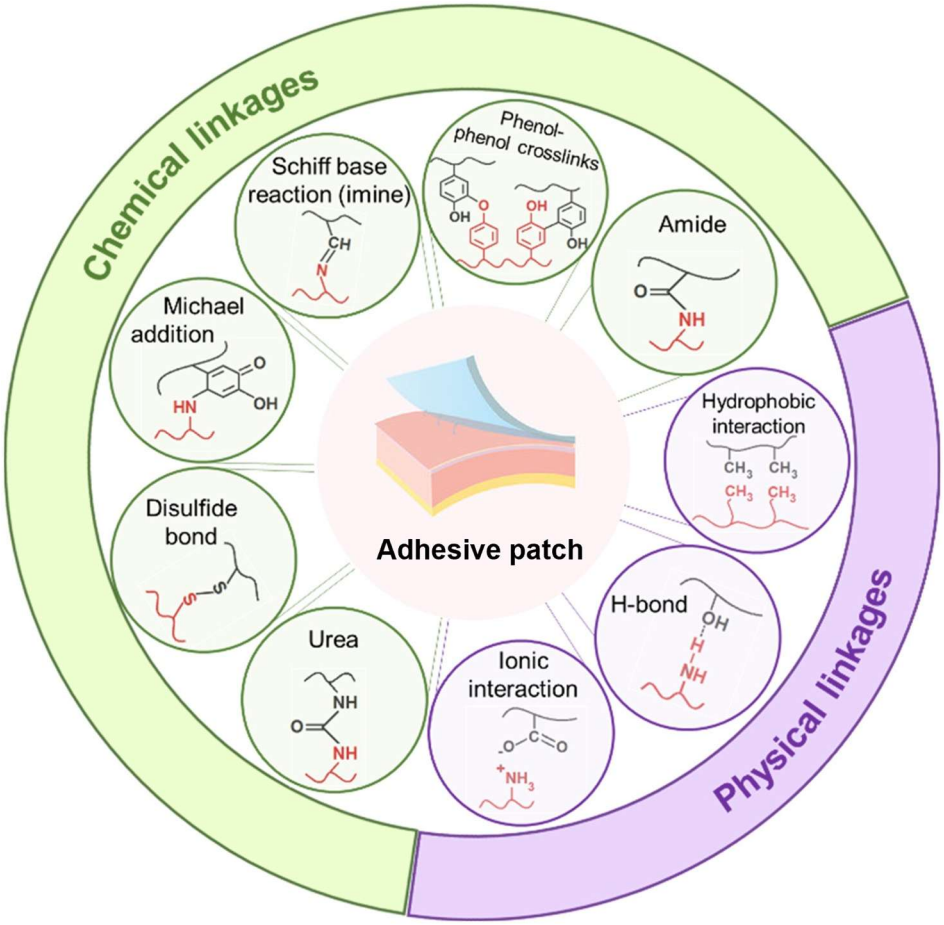

Figure 1-2. Examples of chemical and physical adhesive bonds formed between adhesive material functional groups and tissue active groups. Reproduced with permission from [30], copyright 2019, Elsevier and [31], copyright 2024, Wiley-VCH.

In addition to physical and chemical adhesions, structural factors are also crucial determinants of tissue adhesive performance. As a typical structural factor, mechanical interlock refers to the process by which adhesive materials penetrate into the microscopic crevices, pores, or irregularities of the tissue and then crosslink to generate a physical anchor [23]. Chen et al. synthesized an injectable sulfhydryl-based hydrogel, which could form tight mechanical interlock and enhance the overall wet tissue adhesion. This anchoring effect enhanced the overall adhesive strength by providing resistance to shear and tensile forces, independent of molecular interactions at the

interface. Mechanical interlock is particularly advantageous in wet or bleeding environments, where chemical and physical adhesion may be compromised. By combining mechanical interlock with physical and chemical adhesion, modern tissue adhesives can achieve superior performance, ensuring secure and durable attachment even under challenging physiological conditions.

In summary, the adhesion mechanisms of current tissue adhesives are multifaceted, involving non-covalent and covalent interactions as well as mechanical interlock. The integration of these strategies enables the development of adhesives with enhanced strength for reliable tissue sealing and accurate sensing.

1.1.2 Mechanical properties and adjustment mechanisms

The human body consists of various tissues, each possessing distinct mechanical properties that span a wide range and are finely tuned to their physiological functions. Bone, for instance, is characterized by a high Young's modulus, providing structural support and facilitating body movement. In contrast, soft tissues such as skin exhibit much lower stiffness, enabling flexibility for joint movement. These differences in mechanical performance underscore the critical need to engineer biomaterials with adjustable mechanical characteristics, enabling them to replicate or respond to the mechanical conditions of natural tissues. Otherwise, materials with mechanical properties mismatched to those of the host tissue can result in impaired integration or adverse biological responses, ultimately leading to treatment failure [32]. Furthermore, for sensing applications, the softness of adhesive bandages allows them to conform to the smooth, curvilinear geometry of different tissues [33], and the elasticity of adhesive bandages makes them suitable to serve as the substrates of strain gauge sensors. Additionally, stretchability and elasticity also help to accommodate body movement, reducing artifacts associated with relative motions and ultimately enhancing sensing

accuracy [34]. Therefore, the design and fabrication of bioadhesive bandages should take adequate consideration of their appropriate mechanical properties.

Mechanical properties can be tailored by chemically grafting functional groups [35] or by copolymerizing with other polymers [36, 37], making polymers particularly attractive due to their sufficient mechanical strength and tuneable physicochemical properties [37-39]. For hard tissues, synthetic polymers such as poly(lactic acid) (PLA), poly(glycolic acid) (PGA), and their copolymers (PLGA) are commonly used because of their inherent rigidity and adjustable degradation rates. In contrast, for soft tissues, soft polymers, particularly those based on natural polymers like gelatin, hyaluronic acid, and alginate, are widely employed due to their tissue-like mechanical properties.

Moreover, the mechanical behaviour of polymers can be finely adjusted by polymer concentration, crosslinking method (physical vs. chemical), and the incorporation of secondary networks [40]. For example, interpenetrating polymer networks (IPNs) or composite materials, which combine two or more polymers with distinct mechanical properties, can achieve a balance between strength and flexibility, allowing for the independent tuning of elasticity and toughness. Crosslinking density is another critical parameter, and increasing the degree of crosslinking in polymer networks generally results in higher mechanical strength and reduced elasticity [41], which is desirable for hard tissue applications. For instance, Cao and colleagues prepared a series of sodium alginate hydrogels with gradient crosslinking density, where increasing crosslinking density led to mechanical enhancement [42].

1.1.3 Anti-swelling properties and mechanisms

Polymer materials in aqueous environments inevitably suffer from swelling due to

interactions between polymer chains and water molecules, resulting in an increase in volume. Severe swelling damages the molecular chain structure and significantly affects both adhesive and mechanical characteristics. This deterioration may ultimately cause functional and treatment failure and loss of material stability [21]. Several factors affecting swelling, including the molecular weight, the polymer's hydrophilicity, crosslink density, solvent properties, and environmental conditions [43, 44]. Most hydrogels such as GelMA and PEG-based hydrogels, exhibit a relatively high swelling ratio when applied in wet environments [39, 45], concerning the performance of the adhesives [46, 47]. Therefore, anti-swelling properties are critical for long-term stable applications.

Currently, anti-swelling strategies are generally divided into three main categories: surface hydrophobicity, solvent exchange, and high crosslinking density [48] (**Figure 1-3**A). For instance, Yuan et al. modified a double-hydrophobic coating on the hydrogel surface through surface-confined copolymerization (**Figure 1-3**B). The hydrophobic layer significantly enhanced the water retention capability of the hydrogel, thereby exhibiting outstanding anti-swelling properties [49]. However, surface hydrophobic modification can only be applied to certain materials and primarily inhibits water infiltration, lacking long-term stability. In another study, Jiang et al. fabricated an anti-swelling gel sensor by copolymerizing hydrophilic and hydrophobic monomers in a two-step solvent-exchange strategy [50]. The formed gels exhibited very limited swelling ratios with no obvious volume changes due to aggregation of hydrophobic groups at the material interface, and exhibited excellent underwater sensing properties (**Figure 1-3**C). Nonetheless, solvent exchange strategies often require specific solvents such as dimethyl sulfoxide, which may present potential biological toxicity.

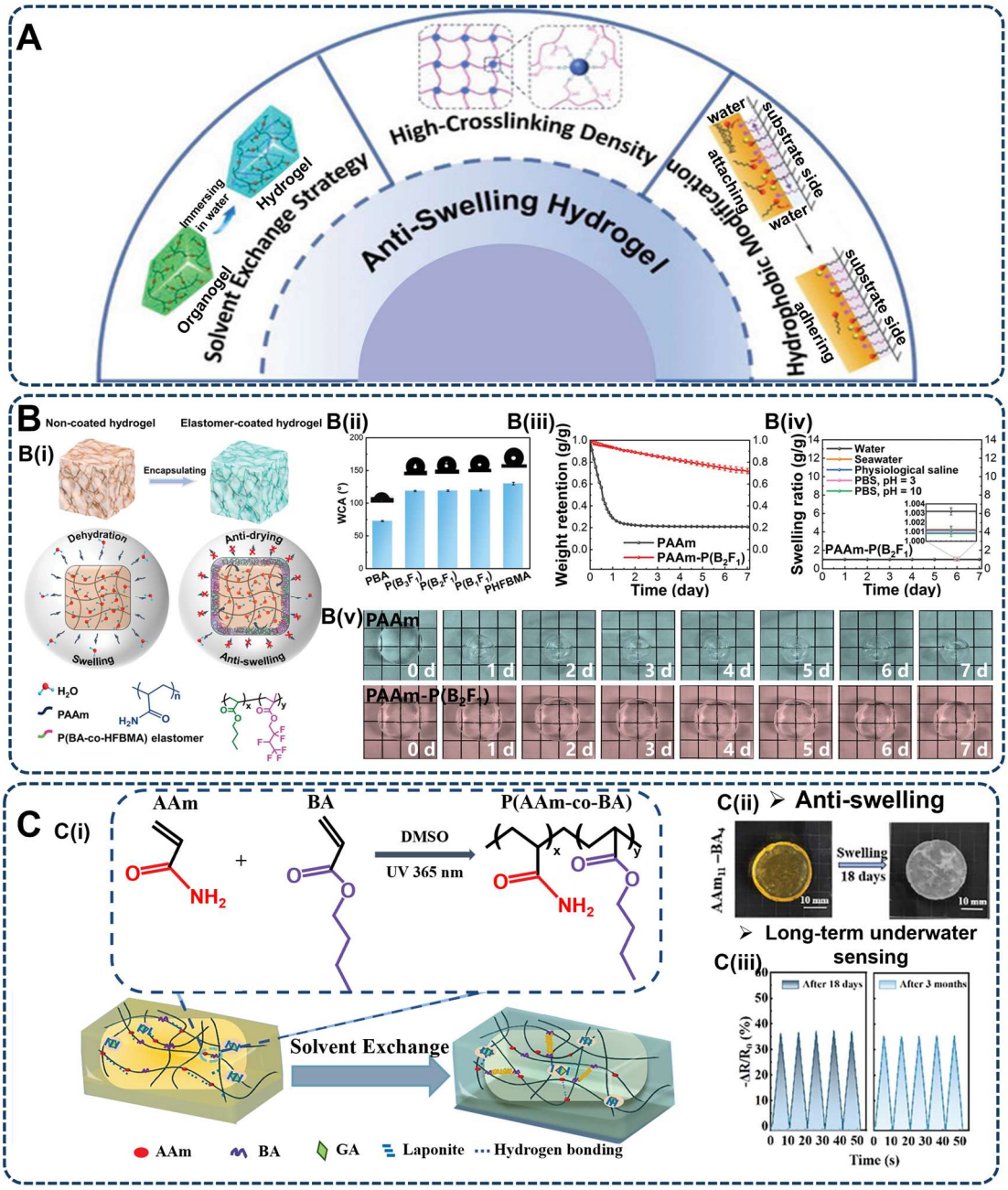

Figure 1-3. Anti-swelling tissue adhesives. (A) Anti-swelling strategies including surface hydrophobic modification, solvent-exchange strategy, and high crosslinking density. Reproduced with permission from [48], copyright 2023, Wiley-VCH. (B) A tissue adhesive fabricated by surface hydrophobic modification strategy, exhibiting outstanding anti-swelling properties in 7 days. Reproduced with permission from [49], copyright 2024, Wiley-VCH. (C) An anti-swelling gel sensor fabricated by solvent-exchange strategy with long-term stable sensing capability. Reproduced with

permission from [50], copyright 2024, Wiley-VCH.

Consequently, primary approach for preparing anti-swelling materials involves high crosslink density, achieved by physical, chemical, or combined means [51]. Physical crosslinking utilizes non-covalent interactions (e.g., hydrogen bonds, van der Waals forces) (**Figure 1-4**B), resulting in a dynamic and reversible process, thus exhibiting relatively low crosslinking density. Therefore, physical crosslinked materials usually undergo serious swelling in wet environment [52]. Chemical crosslinking, on the other hand, utilizes the chemical reactions of crosslinking agents to form covalent crosslinking systems (**Figure 1-4**A), leading to significantly enhanced crosslinking density, and providing excellent anti-swelling effects [53]. Physical/chemical crosslinking combines the aforementioned non-covalent and covalent crosslinking strategies. However, its preparation process is too complex and requires stringent experimental conditions [52], making this strategy unsuitable for biomedical applications.

In summary, employing chemical crosslinking methods with high crosslinking density is an effective approach for preparing anti-swelling materials suitable for long-term stable applications.

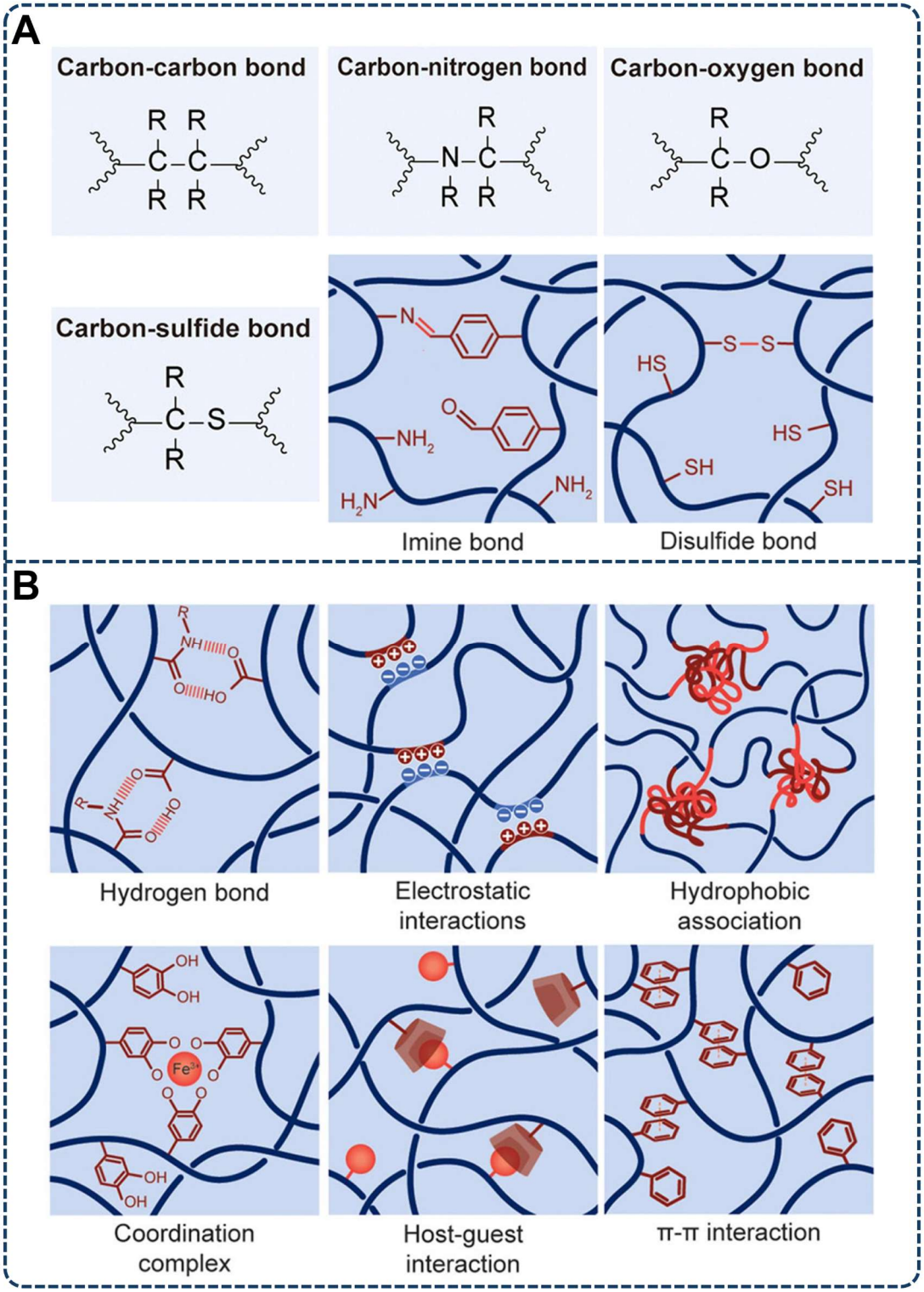

Figure 1-4. Crosslinking strategies of adhesive materials, including (A) chemical and (B) physical crosslinking. Reproduced with permission from [26], copyright 2022, Elsevier.

1.1.4 Adhesive bandages developed for monitoring human physiological activities

Driven by the rapid advancements in biomedical engineering, flexible sensors have become a transformative technology for non-invasive, continuous, and real-time detection of physiological signals. Typical flexible bioelectronic devices are composed of the substrate layer (bottom), interface layer (middle), and active layer (top) (**Figure 1-5**). Each of these layers serves a distinct and essential function, collectively determining the overall performance and functionality of the sensor. The active layer, which serves as the core functional layer, is primarily responsible for signal detection [54]. It is typically constructed from conductive materials, including conductive crystals, liquids, and composites [55-57]. Among them, liquid metals such as gallium-indium eutectic (Ga-In) have attracted significant attention owning to their remarkable stretchability and excellent electrical conductivity [58]. The substrate layer, usually fabricated from soft, stretchable, elastic, and adhesive polymers or hydrogels, provides foundational support for the flexible device against external forces [54] such as bending, stretching, and twisting. Finally, the interface layer acts as a bridge to connect and transmit the signals from the substrate layer to the active layer, facilitating the integration between the two layers.

Adhesive bandages are often used as the substrate layer to integrate the active layers and form a seamless, non-invasive interface with the dynamic and irregular human body, enabling accurate and reliable detection. Conductive hydrogels (such as ion gels) or other stretchable polymers are the most commonly utilized materials [59]. However, ion gels often present toxicity and tend to lose functionality due to water evaporation, raising concerns about their long-term application on the human body [60]. To address these issues, researchers have explored strategies such as copolymerization and side chain modification to engineer stretchable polymers [54] with enhanced

biocompatibility and stability. Currently, various polymer-based substrates are widely investigated as adhesive bandages, including polydimethylsiloxane (PDMS), polyethylene terephthalate (PET), and polyethylenimine [54], due to their softness and elasticity, which are essential for achieving conformal contact with the skin and minimizing discomfort during prolonged wear. However, these materials typically lack adhesive properties and therefore cannot maintain tight and long-term fixation for accurate and durable sensing.

In summary, the fixation of flexible sensors depends on adhesive bandages, which need to take softness, elasticity, and adhesion into consideration. Achieving such a feat requires a careful balance between sensing performance, mechanical compliance, biocompatibility, and long-term stability.

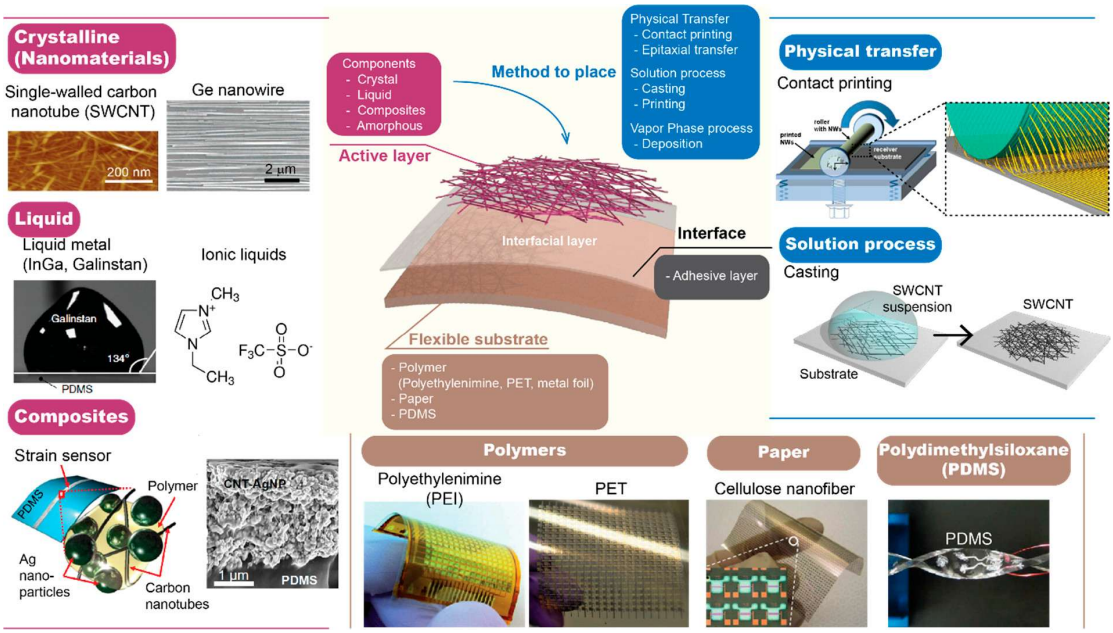

Figure 1-5. Typical functional layers of flexible bioelectronic devices, including the substrate layer, the interfacial layer, and the active layer from bottom to top. Reproduced with permission from [54], copyright 2019, American Chemical Society.

1.2 Materials of wound adhesives and bandages for wound closure and sensing

Recently, tissue adhesives have experienced substantial progress, propelled by the clinical need for minimally invasive, effective, and biocompatible solutions for wound closure and tissue repair. Numerous products are now commercially available for biomedical applications, such as Dermabond®, SurgiSeal®, LiquiBand®, Histoacryl®, and Glubran 2®, all of which have obtained FDA approval for clinical use and feature unique formulations and application profiles. These adhesives, primarily composed of 2-octyl or n-butyl cyanoacrylate, offer distinct advantages, including painless application, reduced need for follow-up visits, and favourable cosmetic outcomes. However, they are generally unsuitable for high-tension, deep, or heavily bleeding wounds and may carry a higher cost compared to traditional closure methods.

Additionally, commercial wearable devices such as VivaLNK, ePatch, S-Patch-Ex, and Mawi Heart Patch were launched for rapid and real-time human health monitoring. However, only a very small number have received FDA approval, and this area remains under development. Furthermore, a wide variety of materials are currently under investigation and development, with both natural and synthetic materials being explored as tissue adhesive bandages, each presenting distinct advantages and limitations.

Natural materials such as protein (e.g., gelatin, collagen) [61, 62], polysaccharides (e.g., hyaluronic acid, alginate, chitosan) [63-65], and polymers like fibrin [66] have long been favoured due to their outstanding biocompatibility and biodegradability. These materials are often derived from components already present in the extracellular matrix, facilitating integration with host tissues and minimizing immune responses. However, a major limitation of these natural adhesives is their poor mechanical properties [65, 67,

68]. For instance, gelatin- and collagen-based adhesives tend to be soft and easily deformed, making them unsuitable for load-bearing applications or long-term stability [67, 69]. Similarly, polysaccharide-based adhesives, while offering good biocompatibility and injectability, often lack the mechanical robustness required for effective tissue adhesion, especially in dynamic or high-stress environments [68]. In addition to weak mechanical properties, most natural adhesives also exhibit limited adhesive strength to tissues. This is primarily due to the lack of functional groups that can establish robust physical or chemical interactions with tissue surfaces. Consequently, their use is often restricted to superficial wounds or as adjuncts to other closure methods. Furthermore, the swelling behaviour of these materials in wet environments can be problematic. High swelling ratios, particularly in hydrophilic polysaccharide-based adhesives, can lead to loss of adhesive contact, mechanical instability, and even treatment failure [68].

To address the limitations of natural materials, synthetic polymers such as polyethylene glycol (PEG) and poly(N-isopropylacrylamide) (PNIPAM) have been extensively developed as tissue adhesives. These materials offer the advantage of tuneable mechanical and physicochemical properties through controlled synthesis and functionalization. However, unmodified synthetic hydrogels frequently exhibit inadequate mechanical strength and limited intrinsic adhesion to biological tissues [61, 70-72], similar to their natural counterparts. Recent strategies to enhance the performance of synthetic adhesives, such as chemical grafting of functional groups (e.g., imine, amide, nitro) [35] and copolymerization with other materials (e.g., gelatin methacryloyl (GelMA) and PLGA-PEG-PLGA [36, 37]), have significantly improve both the mechanical characteristics and the adhesive strength of synthetic polymers [38, 39]. The incorporation of functional groups inspired by biological adhesion mechanisms (e.g., Schiff bases, mussel-like catechols, N-hydroxysuccinimides (NHS), aldehyde groups, and thiol groups [11, 73]), has further advanced the field by enabling

robust covalent or non-covalent bonding with tissue surfaces, which significantly increases adhesive strength even in wet or dynamic environments. However, the fabrication processes for these advanced adhesives are often complex, involving multiple synthesis and purification steps, which can hinder their scalability and clinical translation. Moreover, most hydrogels such as GelMA and PEG-based hydrogels, exhibit a relatively high swelling ratio when applied in wet environments [46, 47], concerning the performance of the adhesives, leading to potential treatment failure.

In summary, recent developments in synthetic tissue adhesives have yielded materials with improved adhesive and mechanical properties through chemical modification and copolymerization. While significant progress has been made, challenges remain, particularly regarding excessive swelling and the complexity of fabrication processes. Therefore, there is still a need for novel bandages that can be fabricated through simple processes, exhibiting softness, elasticity, and adhesive, to adhere firmly to irregular wounds or tissues, broadly adaptable to most hard and soft tissues, and anti-swell in wet and dynamic environments, ensuring robust tissue sealing and long-term accurate sensing.

2. Project aim

Here, we propose a soft, elastic, adhesive, anti-swelling, and biocompatible bandage, termed PLD-PS, fabricated by simply mixing poly(lactide-co-propylene glycol) dimethacrylate (P_7L_2DMA), poly(lactide-co-propylene glycol) (P_7L_2) and a four-arm thiol pentaerythritol tetra(3-mercaptopropionate) (PTM) at room temperature, followed by UV-induced crosslinking (**Figure 2-1**A). The photocrosslinkable and rigid P_7L_2DMA [74] provides mechanical support and facilitates a gentle fabrication process at room temperature [75, 76]. The PTM contains four thiol functional groups in one molecule, which react with the C=C of P_7L_2DMA via thiol-ene click reaction [77] during photocrosslinking [29, 78], and form robust adhesion to tissues through disulfide (S-S) bond formation. The P_7L_2 primarily modulates the mechanical properties of the adhesive by increasing inter-chain friction and energy dissipation through the introduction of hydrogen bonds [79]. Once crosslinked, the bandage will adhere firmly to tissue surfaces by forming hydrogen bonds and disulfide bonds (**Figure 2-1**B). PLD-PS is injectable, enabling fit-to-shape sealing of the complex, non-flat, and irregular geometry of wounds. In addition, PLD-PS can be pre-shaped as an adhesive patch and applied to tissues by gentle pressing, securing the fixation of flexible electronic devices (**Figure 2-1**C). The elastic adhesive PLD-PS bandage can be utilized as a PLD-PS-based sensor capable of detecting finger, wrist, and elbow bending signals by further functionalization by programmable patterning with liquid metal gallium-indium eutectic **(Figure 2-1D)** or transmitting Morse Code information by finger bending **(Figure 2-1E)**.

In this project, we first optimized concentrations of P_7L_2 and PTM, then evaluated the mechanical, adhesive, swelling, and *in vitro* sensing properties of PLD-PS. Additionally, we assessed the *in vitro* cytocompatibility and hemocompatibility of the PLD-PS. We envision that the proposed PLD-PS adhesive bandage will enable rapid and accurate electrocardiogram (ECG) monitoring following implantation. Moreover, we hope that

this work will serve as an inspiration for advanced flexible device substrates.

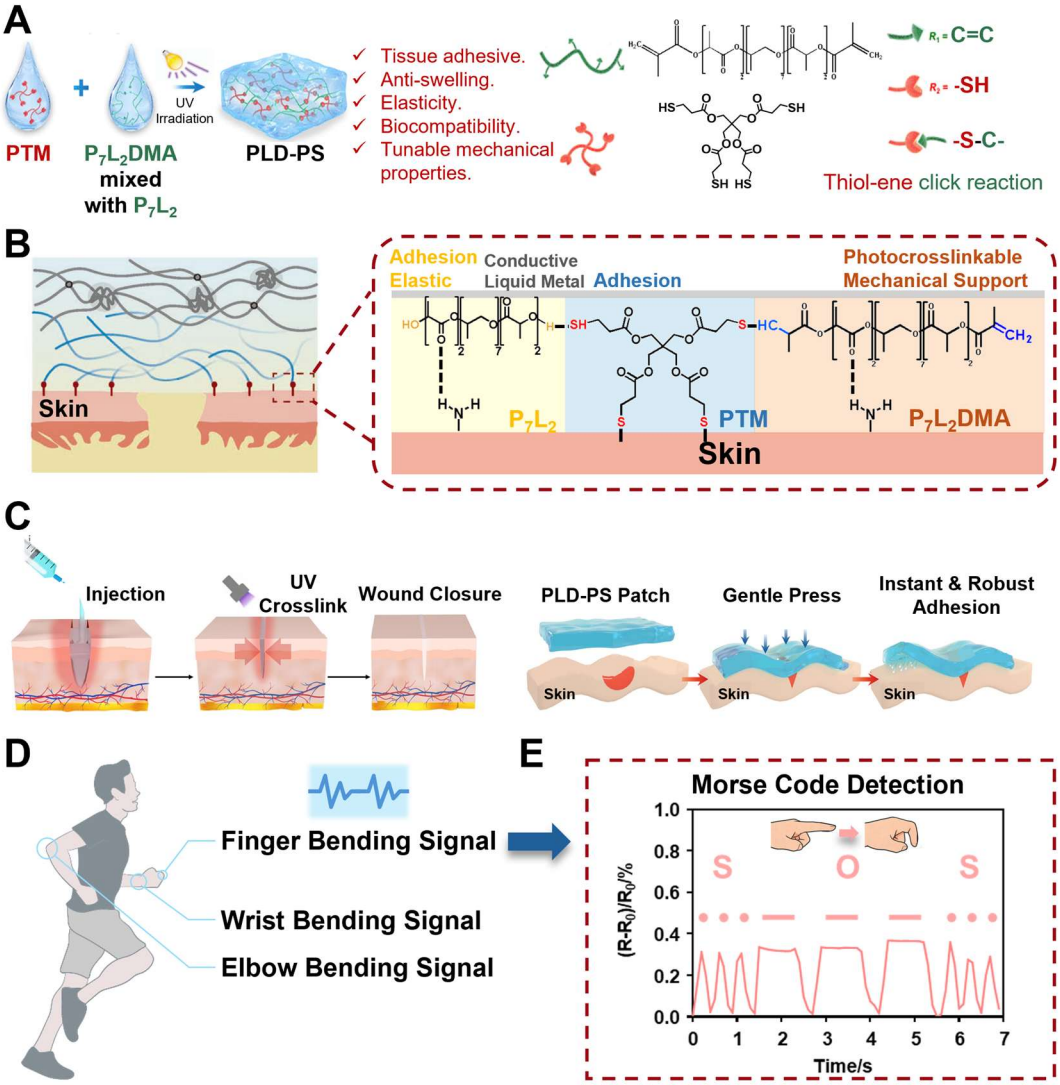

Figure 2-1. Schematic of adhesive bandage PLD-PS and its applications. (A) A simple one-step mixture for the fabrication of PLD-PS with adhesive, elasticity, biocompatibility, as well as anti-swelling and tunable mechanical properties. (B) The photocrosslinkable and rigid P_7L_2DMA provides photocrosslinkability and mechanical support, while PTM provides tissue adhesion. And P_7L_2 primarily modulates the mechanical properties of the PLD-PS. PLD-PS can form hydrogen bonds and disulfide bonds to skin tissues and provide robust adhesion. (C) The PLD-PS can be injectable

and fit to the complex, irregular geometry of skin wounds. PLD-PS can also be pre-shaped as a patch and simply applied to the skin. PLD-PS will be utilized as (D) a PLD-PS-based sensor for finger, wrist, and elbow bending signals detection or (E) transmitting Morse Code information by finger bending.

3. Methodology

3.1 Synthesis, fabrication, and characterization of bioadhesive PLD-PS material

3.1.1 Synthesis of poly(lactide-co-propylene glycol) (P_7L_2)

P_7L_2 was synthesized following our previously reported procedure [80]. Briefly, 500 g PPG (MW 425 g/mol) was mixed with 342.66 g of LA (weight 2.5% more than the theoretical amount) in a 1-L three-necked flask at room temperature with magnetic stirring. The flask was then transferred to an oil bath, which was heated to 110 ºC. A needle was placed beneath the liquid surface to gently introduce nitrogen (N_2) into the flask, and the system was maintained for the removal of free water. Then, the mixture was heated at 135 ºC for 5 hours until the LA was completely molten. Subsequently, the mixture was heated to 155 ºC, and meanwhile, 139.5 μL of catalyser (stannous 2-ethylhexanoate) was added drop-by-drop to the reactants. The mixture was maintained at 155 ºC to initiate the reaction. P_7L_2 was successfully synthesized after 12 hours of reaction overnight. The reaction was terminated by stopping the heating and taking the flask out of the oil bath.

3.1.2 Synthesis of poly(lactide-co-propylene glycol) dimethacrylate (P_7L_2DMA)

P_7L_2DMA was synthesized by grafting carbon-carbon double bonds onto P_7L_2 as described below [80]. Briefly, P_7L_2DMA was synthesized by dissolving 300 g of the synthesized P_7L_2 in 760 mL of dichloromethane (DCM) within a 5 L three-necked flask. The flask was equipped with two constant-pressure dispensing funnels on the left and right necks and a stirring paddle in the centre. With the dispensing funnels closed, stirring was initiated. Two batches of methacryloyl chloride (MAC) and triethylamine (TEA) solutions were prepared as follows: the first batch mixed 165 mL of MAC with 300 mL of DCM, and the second batch mixed 164 mL of MAC with 300 mL of DCM; the first batch of TEA mixed 200 mL of TEA with 250 mL of DCM, and the second batch mixed 200 mL of TEA with 250 mL of DCM. The MAC solutions were loaded

into one funnel and the TEA solutions into the other. A needle was placed under the liquid surface of the MAC solution, and N_2 was gently introduced into the dispensing funnel. The dispensing funnels were then opened, and the MAC and TEA solutions were added dropwise to the P_7L_2 solution at 0 ºC (ice bath) under a N_2 atmosphere to initiate the reaction. After stirring for 24 hours, the reaction was terminated by stopping the stirring and allowing the mixture to return to room temperature.

3.1.3 Purification of P_7L_2DMA

To obtain pure P_7L_2DMA, the synthesized mixture from the previous step was first filtered through a double layer of filter paper in a Brinell funnel to remove large solid impurities. The pH was then adjusted to neutral (confirmed with pH test strips), followed by additional vacuum filtration. The resulting filtrate was evaporated, and each portion of the evaporated product was dried and mixed with methyl tert-butyl ether until complete precipitation of impurities and removal of TEA, MAC, and DCM. The concentrated filtrate was then diluted five-fold with methyl tert-butyl ether and stored overnight at 4 ºC. A silica gel column was preloaded and allowed to settle naturally for one day. The diluted crude product was added to the silica gel column and eluted. All methyl tert-butyl ether eluent was discarded to remove small molecule impurities. When the product began to elute, the solution was collected. Finally, the collected solution was concentrated by rotary evaporation to obtain pure P_7L_2DMA.

3.1.4 Characterization of P_7L_2 and P_7L_2DMA

The ^{1}H nuclear magnetic resonance (NMR) spectroscopy was used to verify the successful synthesis of P_7L_2 and P_7L_2DMA using a Bruker Avance-III 600 MHz FT-NMR Spectrometer System. Specifically, 10 μL of P_7L_2 or P_7L_2DMA was added to 550 μL of deuterated chloroform and mixed thoroughly. The mixture was then transferred to an NMR tube, and spectra were acquired automatically by the machine.

Raman spectroscopy was employed to evaluate the successful addition of C=C onto P_7L_2DMA using an Andor Raman Spectroscopy with 532-nm laser excitation and a Raman shift range of 265-4000 cm^{-1}.

Mass spectroscopy (MS) was used to evaluate the chemical composition of P_7L_2DMA using the Agilent 6540 Liquid chromatography-Electrospray Ionization Quadrupole-Time-of-Flight Mass Spectrometer. Our P_7L_2DMA was dissolved in methanol for further quantification.

3.1.5 Fabrication of bioadhesive PLD-PS material

The bioadhesive poly(lactide-co-propylene glycol) dimethacrylate-poly(lactide-co-propylene glycol)-pentaerythritol tetra(3-mercapto propionate) (PLD-PS) was prepared by directly mixing the components and stirring for 30 minutes at room temperature in the dark, until the mixture changed from cloudy to clear. Subsequently, the preformed mixture (90 wt%) was mixed with 2-hydroxyethyl methacrylate (HEMA) (9 wt%) and diphenyl (2,4,6-trimethyl benzoyl)phosphine oxide (Irgacure 819, 1 wt%, serving as the photoinitiator). The potential air bubbles in the resulting mixture were subsequently removed under vacuum. After degassing, the UV crosslinking box (Scientz 03-II) or UV torch (365 nm) was used to crosslink the bioadhesive PLD-PS.

3.2 Optimization of P_7L_2 and PTM concentration

3.2.1 Fabrication of bioadhesive PLD-PS material with different P_7L_2 or PTM concentration

To optimize the concentration of P_7L_2, PLD-PS samples with fixed PTM concentration

and varying P_7L_2 concentrations were prepared. The fabrication process followed the procedure described in Section 3.2.5.

Table 3-1. Component concentrations for P_7L_2 optimization.

Materials	Group 1	Group 2	Group 3	Group 4	Group 5
P_7L_2DMA	**70%**	**60%**	**50%**	**40%**	**30%**
P_7L_2	**0%**	**10%**	**20%**	**30%**	**40%**
PTM			**30%**		

For the optimization of PTM, based on the optimization of P_7L_2 concentration, a mixture of P_7L_2DMA and P_7L_2 with fixed P_7L_2DMA-P_7L_2 ratio was prepared in advance. PTM was then added to the P_7L_2DMA-P_7L_2 mixture at concentrations varying from 0 wt% to 40 wt%. Fabrication process followed the procedure described in Section 3.2.5.

Table 3-2. Component concentrations for PTM optimization.

Materials	Group 1	Group 2	Group 3	Group 4	Group 5
P_7L_2DMA:P_7L_2			**4:3**		
PTM	**0%**	**10%**	**20%**	**30%**	**40%**

3.2.2 Mechanical properties

Tensile mechanical properties were evaluated at room temperature using a universal testing machine (UTM) fitted with a 100 N load cell, in accordance with the GB/T 1040 standard and a crosshead speed of 1 mm/min. Samples were prepared using a dumbbell-shaped polytetrafluoroethylene mould, with dimensions in the testing region of 16.0 ±

1.0 mm in length, 4.0 ± 0.1 mm in width, and 2.0 ± 0.2 mm in thickness. Briefly, 700 μL of each sample was dispensed into the mould for testing. A vacuum desiccator was then used to remove air bubbles from the material. After degassing, the samples were taken out and covered with a glass slide onto the surfaces of the samples to avoid oxygen. Following UV crosslinking, the glass slides were detached, and the samples were ready for testing. Young's modulus, tensile strength, fracture stress, and elongation at break were measured. Young's modulus was characterized as the slope of the stress-strain curve within the elastic deformation region (MPa), fracture stress as the highest stress sustained by the material prior to failure (MPa), and elongation at break as the strain at failure (%).

Compressive properties were tested at room temperature using a UTM with a 100 kN load cell, also following the GB/T 1040 at a loading rate of 1 mm/min. Cylindrical specimens (Ø 6 mm × 6 mm) were fabricated using a PDMS mould, employing a sample preparation process analogous to that used for the tensile testing. The compressive modulus was determined as the slope of the stress-strain curve within the elastic region and reported in MPa.

3.2.3 Adhesive properties

Lap-shear tests and 180° peeling tests were performed to evaluate the adhesive properties of the adhesive PLD-PS materials on tissues substrates. These evaluations utilized a UTM equipped with a 100-N load cell at room temperature following ASTM F2255 and ASTM F2256 standards, respectively (1 mm/min separation speed). Fresh porcine skin was sourced from the market, thoroughly rinsed with water to remove blood and other contaminants, and trimmed with a scalpel to remove excess hair and subcutaneous fat, resulting in samples approximately 3 mm thick. Additionally, to assess anti-leakage properties, burst pressure was measured under both air and PBS

conditions using PDMS and porcine skins, in accordance with ASTM F2392-04 at room temperature.

For lap-shear tests, porcine skin was cut into rectangles measuring 25 mm × 50 mm and stored in PBS at 37 ºC prior to testing. After adhesive PLD-PS preparation, the skin samples were removed from PBS and gently blotted with a paper towel to remove excess surface moisture. Then, 200 μL of PLD-PS was applied to the surface of the porcine skin, followed by UV irradiation for 5 minutes. The adhesion area was maintained at 25 mm in width and 50 mm in length. After crosslinking, one side of the crosslinked sample was adhered to a piece of porcine skin, while the opposite side was fixed to another piece of porcine skin using ethyl 2-cyanoacrylate glue (Deli) to ensure that the measured adhesive strength reflected the bond between the *in situ*-formed adhesive and the porcine skin. The back of the porcine skin was fixed to a cardboard using ethyl 2-cyanoacrylate glue to prevent skin deformation during tensile testing and measurement error. The adhesive strength was calculated using the following formula:

$$\text{Lap-shear strength} = \frac{F}{w \times l}$$

where F is the maximum stress recorded during the test, w is width of the adhesion area, and l is the length of the adhesion area.

For 180° peeling tests, fresh porcine skin was cut into rectangles measuring 25 mm × 150 mm and immersed in PBS at 37 ºC for storage prior to testing. After adhesive preparation, the skin was removed from PBS and excess water was blotted away. Then, 1.5 mL of PLD-PS adhesive was added to the porcine skin surface, followed by UV irradiation for 5 minutes to achieve crosslinking. The adhesion area was standardized to 25 mm × 100 mm. After crosslinking, one side of the adhesive sample was adhered to a piece of porcine skin, while the other side was attached to another piece of porcine skin using an ethyl 2-cyanoacrylate glue (Deli). To prevent deformation and ensure

accurate measurement during testing, the back of the porcine skin was affixed to cardboard using ethyl 2-cyanoacrylate glue. The interfacial toughness was calculated using the following formula:

$$\text{Interfacial toughness} = \frac{2 \times F}{w}$$

where F is the average stress measured between displacement of 25 mm and 150 mm, and w is the width of the specimen.

For burst pressure tests, a Ø 3 mm hole was created at the testing substrate (both PDMS and porcine skin were used) centre using a puncher. PLD-PS was then applied to cover the hole, followed by UV irradiation for 5 minutes. Burst pressure was measured by manually squeezing a syringe (containing air or PBS) attached to the instrument and recording the maximum pressure before material failure.

3.3 Swelling property

The swelling properties of the bioadhesive PLD-PS material were evaluated in PBS solution. First of all, 0.25 g of material was added to a preformed cylindrical PDMS mould (Ø 10 mm × 1 mm). A vacuum desiccator was used to degas the material for 15 minutes to remove air bubbles. After degassing, the samples were removed and covered with a glass slide to avoid oxygen. UV crosslinking was performed for 5 minutes, after which the glass slide was detached, and the samples were collected. The samples were weighed (denoted as W_0) and transferred to individual 15 mL centrifuge tubes. Each tube was filled with 10 mL of PBS, and the samples were incubated on a shaker at 37 ^{o}C, with PBS refreshed daily. At designated time points, PBS was removed, excess water of the samples was blotted away, and the samples were weighed using a precision balance (denoted as W_t). The swelling ratio was calculated using the following formula:

$$\text{Swelling ratio (\%)} = \frac{W_t - W_0}{W_0} \times 100\%$$

where W_t is the sample weights at each time point, and W_0 is initial weight before immersion.

As swelling may affect the mechanical performance of materials, the tensile mechanical properties of the samples after swelling were also assessed. Dumbbell-shaped tensile specimens were prepared as described in the previous section (3.3.2). Each specimen was placed individually in a separate petri dish, and 10 mL of PBS was added to ensure complete immersion at 37 ºC, with PBS refreshed daily. At designated time points, the PBS was removed, the excess water of each specimen was blotted away, and tensile testing was carried out. Tensile properties of the samples were evaluated using a UTM equipped with a 100 N load cell at room temperature, in accordance with the GB/T 1040, at a 1 mm/min crosshead speed.

3.4 Water contact angles (WCA)

Thin films were prepared according to our previous work [81]. Specifically, 0.03 g of material was spread onto a glass slide (22 × 26 mm). Then, a 3-(trimethoxysilyl)propyl methacrylate (TMSPMA)-treated coverslip (22 × 26 mm) was then used to cover the above glass slide. A UV light box (Scientz 03-II) was used to photocrosslink the sample. After crosslinking, the glass slide was detached, and a thin film was ready for WCA test. A small droplet of water was lightly dropped on the surface of the material, and WCA was measured using JC2000D_ContactAngle software, which was also used to analyse the WCA data.

3.5 Water Vapor Transmission Rate (WVTR)

The water vapor permeability of the synthesized polymers (P_7L_2DMA, PLD-P, PLD-PS), and a widely used flexible electronic substrate material PDMS was characterized by measuring the WVTR according to the ASTM E96 standard [75]. Circular specimens (Ø=30 mm) were prepared using PDMS moulds. Then, these samples were used to seal the centrifuge tubes (Ø=29 mm) containing 25 mL of deionized water. The assemblies were placed in the incubator at 37 ºC with 35% humidity. The initial mass was recorded, and the subsequent water loss at different time points was also weighted for the WVTR calculation. The WVTR was calculated using the following formula:

$$\text{WVTR (g/hour/}mm^2\text{)} = \frac{M_t - W_0}{A \times t} \times 100\%$$

where M_0 is initial weight, M_t is the sample weights at each time point, A is the exposed surface area of the sample and t is the time.

3.6 Degradation property

The degradation of the bioadhesive PLD-PS material was evaluated in deionized water (ddH_2O). To prepare the samples, 2.5 g of the material was first added to a cylindrical PDMS mould (Ø 3 cm × 3 mm). A vacuum desiccator was then used to degas the material for 15 minutes to remove air bubbles. After degassing, the samples were taken out and covered with a glass slide, followed by UV crosslinking for 5 minutes. After crosslinking, the glass slide was detached, and the samples were collected and weighed (denoted as W_0). Each sample was then transferred to an individual well of a 12-well plate (one sample per well). 10 mL of ddH_2O was added to each well, and the samples were incubated on a shaker at room temperature. At designated time points, the PBS was removed, and excess water of each specimen was blotted. The samples were dried at 80 ºC for 2 days to ensure complete removal of water. The completely dried specimen was then weighed using a precision balance (denoted as W_t). The following formula was used to calculate the degradation ratio:

$$C/C_0\ (\%) = \frac{W_t}{W_0} \times 100\%$$

3.7 *In vitro* biocompatibility

A thin film was first prepared according to our previous work [81] and followed the procedure described in Section 3.5. The formed films (attached to the coverslips) were then cut into ~1-cm^2 pieces and transformed to a petri dish (diameter 35 mm). Before testing, each sample was subjected to UV irradiation for 1 hour and subsequently washed three times with sterile PBS to remove potential contaminants. L929 cells were used in this experiment and cultured in DMEM medium according to ISO 10993-5. PBS was used to wash and clean the cells, and trypsin was used for cell digestion. Mouse fibroblast L929 cells were seeded in 6-well plates at a density of 0.8×10^4 cells/cm^2. After cell adhesion, the samples were gently placed in the centre of the wells. After incubation for 1 and 3 days, the cells were prepared for Live/Dead and CCK-8 staining.

For Live/Dead staining, cell viability was assessed using a commercial live/dead kit. Briefly, the culture medium was aspirated with a micropipette from each well, and cells were gently washed with PBS, which was then removed. The live/dead working solution was prepared by diluting both Calcein-AM and PI at a ratio of 1:1000 in DMEM medium. Equal volumes of the working solution were added to each well, and the cells were incubated 30 minutes at 37 ^oC in the dark. After incubation, the working solution was removed, and the cells were washed three times with PBS. Cell viability was observed using a Nikon AXE laser confocal microscope. Live cells fluoresced green, while dead cells fluoresced red. Image J was used to quantify the cell viability by calculating the proportion of green cells relative to that of the total number of cells.

For CCK-8 staining, cell proliferation was evaluated after 1 and 3 days of incubation using a commercial CCK-8 kit (10%). CCK-8 reagent was diluted with DMEM medium at a ratio of 1:10 to obtain a 10% working solution. Equal volumes of the CCK-8 working solution were added to each well to fully cover the bottom, and the cells were incubated for 2 hours at 37 ºC in the dark. After incubation, the solution from each well of the 6-well plate was transferred to a 96-well plate (each sample was distributed into four sub-wells of equal volume). The absorbance at 450 nm was measured using a BioTek Synergy H1 multimode microplate reader. Cell proliferation was calculated using the following formula:

$$\text{Cell proliferation (\%)} = \frac{\text{Abs}_{\text{material}} - \text{Abs}_{\text{blank}}}{\text{Abs}_{\text{control}} - \text{Abs}_{\text{blank}}} \times 100\%$$

where $\text{Abs}_{\text{blank}}$ is the absorbance of the blank medium, $\text{Abs}_{\text{material}}$ and $\text{Abs}_{\text{control}}$ refer to the absorbance of cells cultured with the material extract, and the cells cultured with control medium DMEM, respectively.

3.8 *In vitro* hemostasis properties

For the hemostasis test, commercial mouse blood (Pythonbio) was used to determine the clotting time and blood clotting index (BCI) of the adhesives, with commercial thrombin serving as the positive control. Briefly, 10 μL of either the adhesive material or thrombin was used to coat the bottom of a 96-well plate. Prior to testing, each well was filled with 100 μL of DMEM and soaked for 2 days to remove impurities or contaminants. After soaking, the medium was removed, and the materials were washed three times with PBS to ensure complete removal of DMEM. Sodium citrate anticoagulated rat blood was mixed with 10% calcium chloride and vortexed for 10 seconds to activate coagulation. Then, 50 μL of the activated blood was added to each well. At various time points, uncoagulated blood was washed by 5 mL of PBS, while clotted blood still remained in the well. Blood clotting time was defined as the time required to form a firm blood clot in each well. The absorbance of the aforementioned

collected PBS containing unclotted blood at 540 nm was measured by a BioTek Synergy H1 multimode microplate reader. The BCI was calculated through the following formula:

$$\text{BCI (\%)} = \frac{\text{Abs}_{\text{sample}}}{\text{Abs}_{\text{control}}} \times 100\%$$

where $\text{Abs}_{\text{sample}}$ is the absorbance of the aforementioned PBS wash from the test sample, and $\text{Abs}_{\text{control}}$ is the absorbance of the 50 μL of blood dissolved in 5 mL of PBS.

For the hemolysis test, commercial mouse blood (Pythonbio) was utilized to determine the hemolysis ratio. Briefly, 500 μL of material was used to coat the bottom of the 24-well plate. Prior to testing, each well was filled with 500 μL of DMEM and soaked for 2 days to remove impurities or contaminants. After soaking, the medium was removed, and the wells were washed three times with PBS to ensure complete removal of DMEM. During the test, PBS was used as the negative control, and 0.1% Triton X-100 was used as the positive control. Red blood cells (RBC) were collected by centrifuging (8000 rpm, 10 minutes) and washed three times with PBS. Then, 500 μL of RBC were added to the surfaces of the PLD-PS samples or mixed with the control samples by gently pipetting and incubated at 37 ºC for 1 and 8 hours. After incubation, the RBC were collected and centrifuged (8,000 rpm, 10 minutes), and the absorbance of the supernatant was measured at 540 nm using a BioTek Synergy H1 multimode microplate reader. The hemolysis ratio was calculated through the following formula:

$$\text{Hemolysis ratio (\%)} = \frac{A_h - A_p}{A_t - A_p} \times 100\%$$

where A_h is the absorbance of the supernatant from the sample, A_p is the absorbance of the PBS negative control, and A_t is the absorbance of the Triton X-100 positive control.

3.9 Sealing properties on different organs

The *in vitro* adhesion of PLD-PS to biological tissues, including intestine, liver, and kidney, was evaluated. For intestine sealing, a Ø 1 mm perforation was first created in the porcine intestine. PLD-PS was applied to the surface of the perforation, followed by UV irradiation to induce crosslinking. For liver and kidney sealing, a 2-cm incision was made with a scalpel, after which PLD-PS was applied and crosslinked using UV irradiation.

3.10 Sensing properties

A PLD-PS patch (20 × 15 × 1 mm^3) was fabricated and patterned, then connected to a conductive tape. The relative resistance changes ($\Delta R/R_0$) of the PLD-PS-based sensor under different strains were recorded using a source meter (Keithley 2400) in conjunction with a customized UTM (Zolix) connected to the conductive tape. The resistance of the PLD-PS-based sensor was continuously monitored throughout the entire stretching process. The $\Delta R/R_0$ was calculated according to the following formula:

$$\frac{\Delta R}{R_0}(\%) = \frac{R_t - R_0}{R_0} \times 100\%$$

where R_t is the resistance after stretching, R_0 is the original resistance of the PLD-PS-based sensor, and ΔR is the resistance change during stretch.

The relative gauge factor (GF) was applied to evaluate the accuracy of the hydrogel during stretching. GF was calculated according to the following formula:

$$GF = \frac{\Delta R / R_0}{\Delta L / L_0}$$

where the ΔR and R_0 are the resistance changes after stretch and the original resistance, and the ΔL and L_0 are the elongation after stretch and the original length of the PLD-PS-based sensor.

The sandwich-structured PLD-PS-based sensor was fabricated through a multi-step process. A PLD-PS patch (20 × 15 × 0.5 mm^3) was first prepared, and its surface was patterned with liquid metal Ga-In. The PLD-PS patch was then transferred to another mold (20 × 15 × 1 mm^3), onto which an additional layer of PLD-PS was cast. After UV crosslinking, the sandwich-structured PLD-PS-based sensor was successfully fabricated.

For cyclic sensing tests at different strains (5%, 10%, 15%, and 20%), an LCR meter (Tonghui) was used in conjunction with a cyclic stretch machine. The sandwich-structured PLD-PS-based sensor was placed on the cyclic tensile platform, where the maximum strain was fixed during the whole testing process. The LCR meter was connected to the sensor, and the resistance of the sensor during cyclic movement was recorded. The cyclic sensing performance after immersion in PBS for one day was also recorded to assess the consistency of the sensor.

To monitor body movements, the sensor was adhered to various joints, including the wrist, elbow, and finger. As in previous tests, the LCR meter was connected to the sensor, and the resistance changes during body movements were recorded.

For Morse code detection, the sensor was adhered to the index finger. The LCR meter monitored resistance changes during finger bending at different frequencies, enabling the transmission of Morse code messages.

3.11 Statistical analysis

GraphPad was used to perform the statistical analysis. Unless otherwise specified, all experiments were performed with at least three replicates. Data are presented as mean ± standard deviation (SD). Statistical differences were assessed using one-way ANOVA. A p-value $\leqslant$ 0.05 was considered statistically significant, with significance levels indicated as follows: *p$\leqslant$ 0.05, **p$\leqslant$ 0.01, ***p$\leqslant$ 0.001.

4. Results and Discussion

4.1 Synthesis, fabrication, and characterization of P_mL_nDMA material

We first synthesized P_7L_2DMA, where 7 and 2 represent the unit lengths of PPG and LA, respectively. At the beginning, the chemical structures of the initial materials (PPG, LA, and MAC) were first verified. After synthesis and purification, the chemical structures of the synthesized P_7L_2 and P_7L_2DMA were confirmed by ^1H NMR spectroscopy. As shown in **Figure 4-1**, the -CH peaks of P_7L_2 at approximately 5.15 ppm (k) and 1.59 ppm (j) were at the similar chemical shift as the -H peak of LA at 5.15 ppm (e) and the -CH peaks of LA at approximately 1.59 ppm (d), which indicated the successful grafting of LA onto PPG. The ratio of PPG to LA was calculated by the area of peak h, peak j, and peak k, confirming the synthesis of P_7L_2. By calculating the area of the -OH peak of P_7L_2 at approximately 3.95 ppm (l), the grafting ratio of LA to PPG was determined to be 95.5%, further validating the reaction. The single peak of P_7L_2 at approximately 4.35 ppm was considered to be the unreacted LA. Additionally, as for P_7L_2DMA, the C=C peaks at approximately 5.59 ppm (n) and 6.15 ppm (n), as well as the -CH peaks at approximately 1.90 ppm (m) were at the same chemical shift as the C=C peaks of MAC at approximately 6.19 ppm (f) and the -CH peaks of MAC at approximately 1.90 ppm (g), verified the methacrylation of P_7L_2, indicating successful synthesis of P_7L_2DMA. By calculating the area of the C=C peaks of P_7L_2DMA, the synthesis efficiency of the methacrylation of P_7L_2 was calculated to be 96.75%.

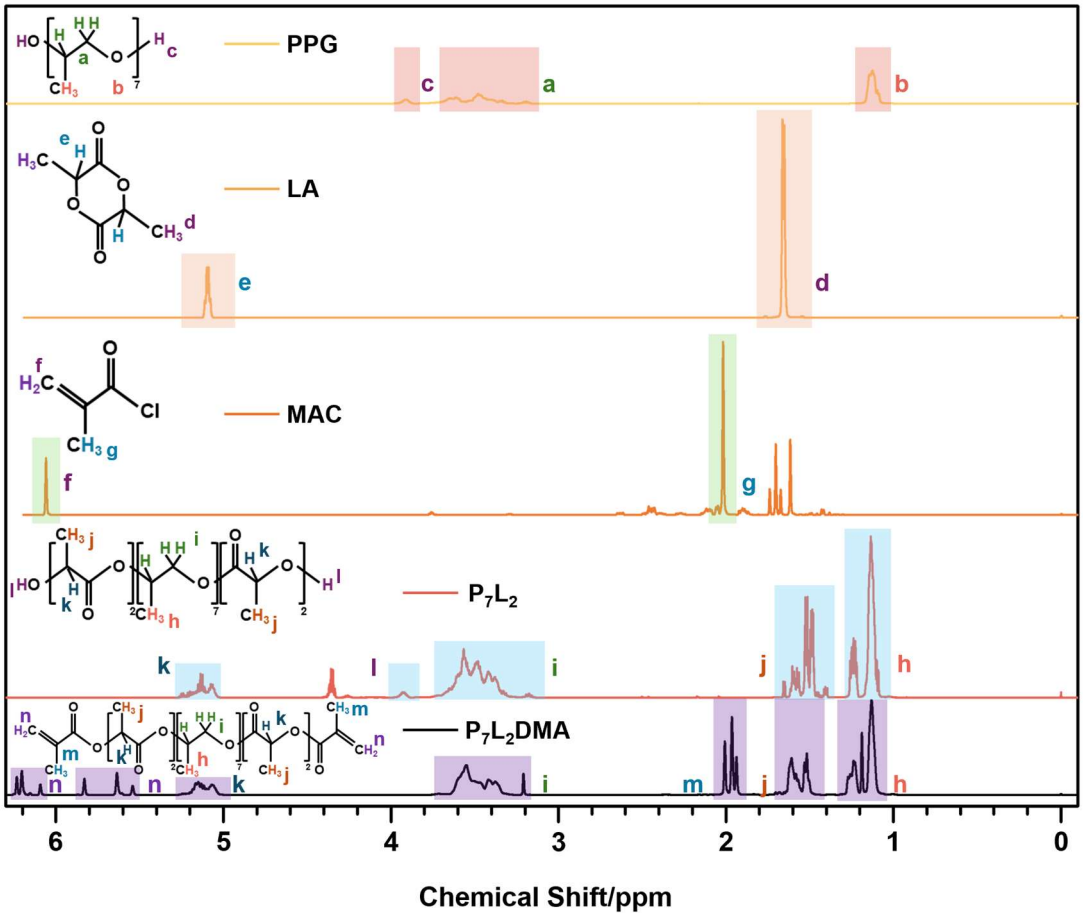

Figure 4-1. ^{1}H NMR spectra of PPG, LA, MAC, and the synthesized P_7L_2 and P_7L_2DMA.

Further Quadrupole-TOF-MS was conducted to verify the chemical structure of our synthesized P_7L_2DMA (**Figure 4-2**). The mass to charge peak distances between 664.3917 Da and 808.4344 Da (purple symbol), 694.4747 Da and 838.5178 Da (red symbol), and 722.4338 Da and 866.4756 Da (blue symbol) all corresponded to the LA chain segment (molecular weight: 144.13), indicating the successful grafting of LA.

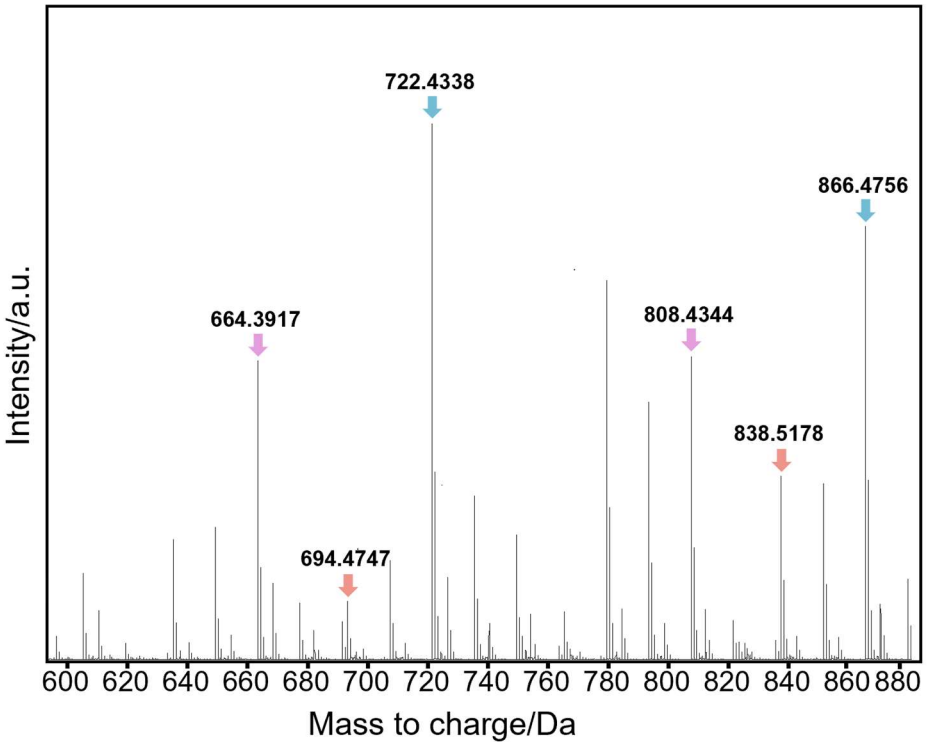

Figure 4-2. Quadrupole-TOF-MS spectra of our synthesized P_7L_2DMA.

In addition, Raman spectra of P_7L_2 and P_7L_2DMA were also obtained (**Figure 4-3**). The single peak observed at 1640 cm^{-1} corresponded to the C=C stretching vibration of the methacrylate, as reported in previous studies [80], further confirming the successful grafting of methacrylate onto P_7L_2.

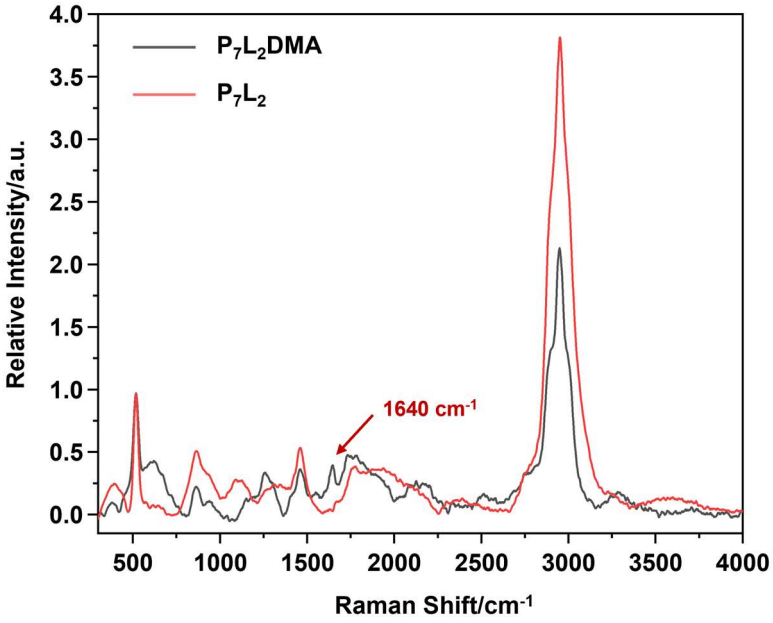

Figure 4-3. Raman spectra of P_7L_2 and P_7L_2DMA.

4.2 Optimization of PLD-P material

4.2.1 Optimization of P_mL_nDMA substrate

We subsequently evaluated the tensile mechanical properties of P_7L_2DMA and $P_{68}L_8$DMA after crosslinking. As shown in **Figure 4-4**, P_7L_2DMA exhibited a higher tensile modulus of approximately 10 MPa, which is suitable for most hard tissues (such as colon, urinary bladder, and muscle) and soft tissues (such as liver, heart, and lung) [82], particularly after further incorporation with PTM. In contrast, $P_{68}L_8$DMA displayed a lower tensile modulus of approximately 260 kPa, making it suitable only for soft tissues. The reported modulus of natural skin ranges from several kPa to several MPa [83, 84]. Specifically, the natural dermis has a modulus of approximately tens of kPa, while the epidermis has a modulus of approximately several MPa [85]. Therefore, P_7L_2DMA was more suitable for skin and most other tissues, and was selected for subsequent experiments.

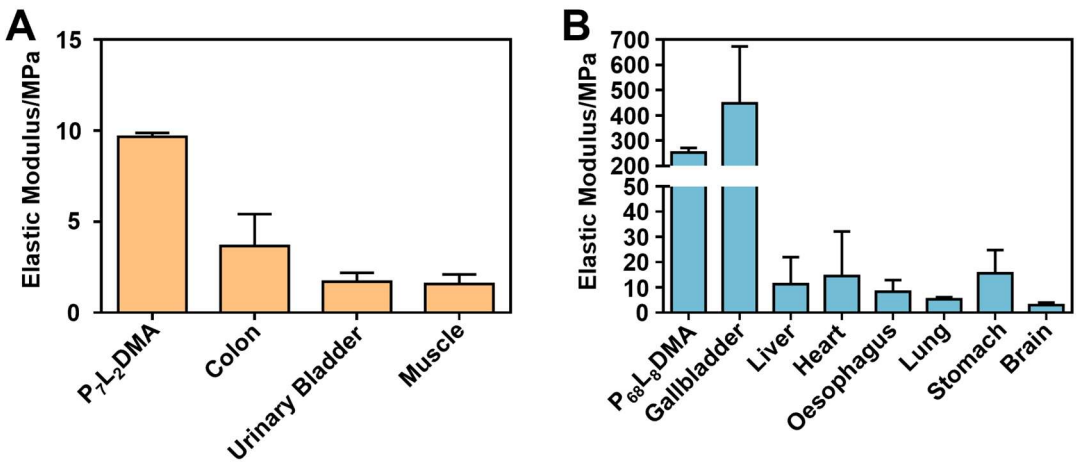

Figure 4-4. Young's modulus of P_7L_2DMA, $P_{68}L_8$DMA as well as human hard and soft tissues.

4.2.2 Optimization of P_7L_2 concentration

Since P_7L_2 can modify the mechanical properties and provide tissue adhesion, as discussed in the previous chapter, the optimization of P_7L_2 was conducted by evaluating the mechanical and adhesive properties, as well as burst pressure tolerance. In this part of the experiment, the PTM concentration was fixed at 30%, while the P_7L_2 concentration was varied from 0% to 40% to determine the optimal formulation. P_7L_2DMA and PTM mixture with no P_7L_2 incorporation was designated as PLD-S. Eventually, the group exhibiting the most favourable properties was selected, and the corresponding P_7L_2DMA to P_7L_2 ratio (designated as PLD-P) was used in subsequent experiments.

Figure 4-5 presents the macroscopic images of the PLD-PS samples with different P_7L_2 concentrations subjected to compression. Without P_7L_2, the material behaved as a rigid solid and was difficult to compress. With the addition of 10% P_7L_2, the material becomes significantly softer. Further increases in P_7L_2 content result in progressive

softening of the material. These results indicated that PTM doping alone did not significantly alter the mechanical properties, and that substantial improvements occurred only when both P_7L_2 and PTM were present. Additionally, the material demonstrated excellent elasticity throughout the compression process, and the material returned to its original shape upon stress relief. This property contributed to enhanced sensing performance and data stability of the sensors.

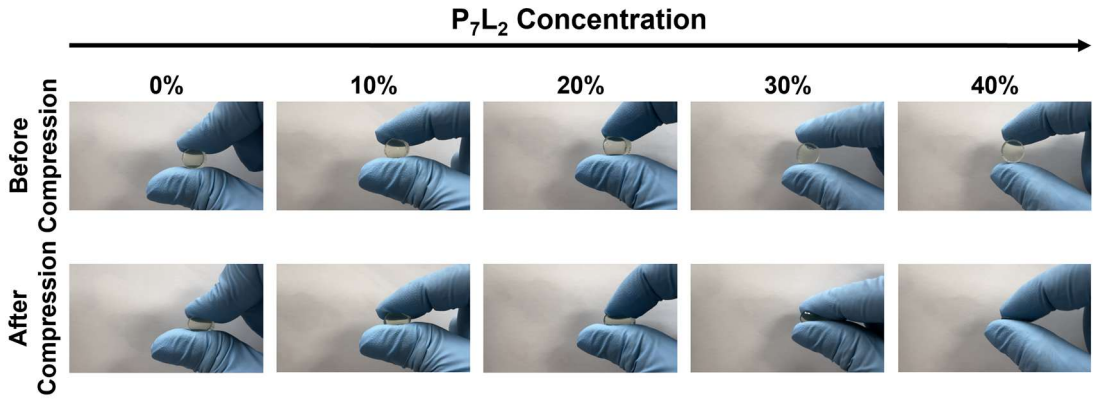

Figure 4-5. Images of PLD-PS with different P_7L_2 concentrations under compression.

To address the phenomenon described in the previous section, tensile mechanical tests were conducted to quantitatively evaluate the mechanical properties of the materials. As shown in **Figure 4-6**, all materials exhibited elasticity. Furthermore, the tensile modulus of the materials decreased significantly with increasing P_7L_2 concentrations, from 4.300 ± 0.452 MPa (0% P_7L_2) to 0.112 ± 0.004 MPa (40% P_7L_2). The fracture stress gradually decreased from 0.702 ± 0.200 MPa (0% P_7L_2) to 0.063 ± 0.024 kPa (40% P_7L_2), while the elongation at break increased from 15.954 ± 4.833% (0% P_7L_2) to 29.808 ± 5.686% (40% P_7L_2) (**Table 4-1**). Notably, the groups containing 20%, 30% and 40% P_7L_2 exhibited mechanical properties that were comparable to human skin, which is crucial for achieving conformal adhesion to tissue [83].

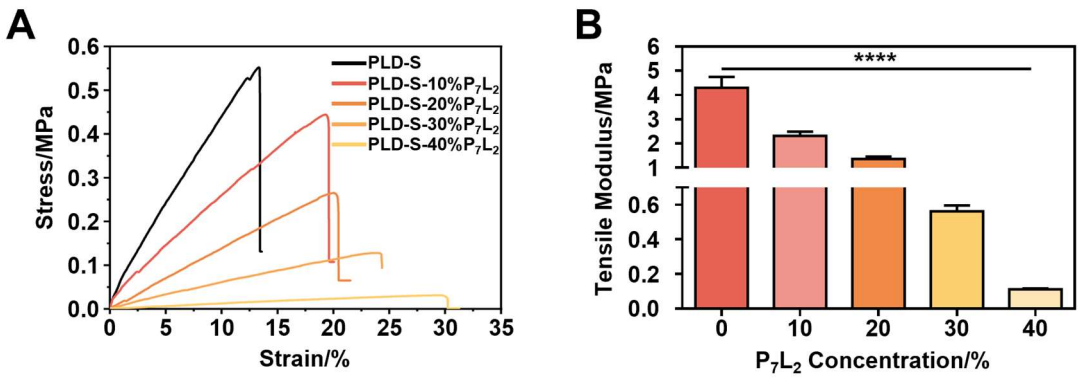

Figure 4-6. Tensile properties of PLD-PS with increasing P_7L_2 concentration. (A) The stress-strain curve, and (B) the tensile modulus.

Table 4-1. Tensile mechanical properties of PLD-PS with different P_7L_2 concentrations.

Materials	Modulus/MPa	Fracture Stress/MPa	Fracture Strain/%
PLD-S	**4.300 ± 0.452**	**0.702 ± 0.200**	**15.954 ± 4.833**
PLD-S-10% P_7L_2	**2.320 ± 0.175**	**0.420 ± 0.090**	**18.283 ± 4.460**
PLD-S-20% P_7L_2	**1.368 ± 0.034**	**0.259 ± 0.070**	**19.528 ± 5.566**
PLD-S-30% P_7L_2	**0.562 ± 0.034**	**0.092 ± 0.029**	**17.304 ± 5.272**
PLD-S-40% P_7L_2	**0.112 ± 0.004**	**0.034 ± 0.006**	**29.808 ± 5.686**

Next, the adhesive properties of the material were further evaluated by the lap-shear method. Porcine skin was selected as the substrate due to its physiological structure [86] and mechanical properties [87], which closely resemble those of human skin and make it a common model in bioadhesive research. P_7L_2 facilitates material adhesion by

forming hydrogen bonds with tissue. As shown in **Figure 4-7**, the adhesive strength increased from 6.06 ± 0.96 kPa for 0% P_7L_2 to 58.00 ± 4.52 kPa for 30% P_7L_2. For comparison, the reported adhesive strengths of fibrin glue and other commercial adhesives are 1-10 kPa and 10-100 kPa, respectively [18]. The adhesive strength of our material exceeded that of fibrin glue and was comparable to commercial adhesives. However, the adhesion strength of the 40% P_7L_2 group was significantly reduced, likely due to exceeding the maximum stress the material could withstand. Its measured adhesion strength (26.779 ± 1.184 kPa) was similar to the measured fracture stress (0.034 ± 0.006 MPa) in **Table 4-1**, which corroborated the observation.

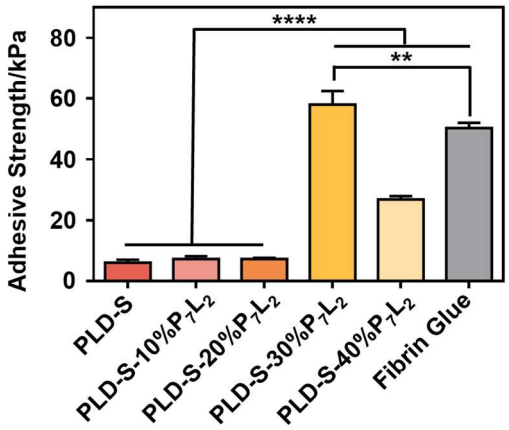

Figure 4-7. Adhesive strength of PLD-PS with different P_7L_2 concentrations and commercial fibrin glue on porcine skin.

The adhesive performance of the material on porcine skin after soaking in water for one day was also assessed. **Figure 4-8** shows the photographs of PLD-PS with varying P_7L_2 concentrations adhering to porcine skins. All adhesives adhered firmly to porcine skin on day 0, except for the 0% P_7L_2 group, which failed due to mechanical mismatch. After soaking in PBS for one day, only the 30% and 40% P_7L_2 groups remained adhered to

porcine skin.

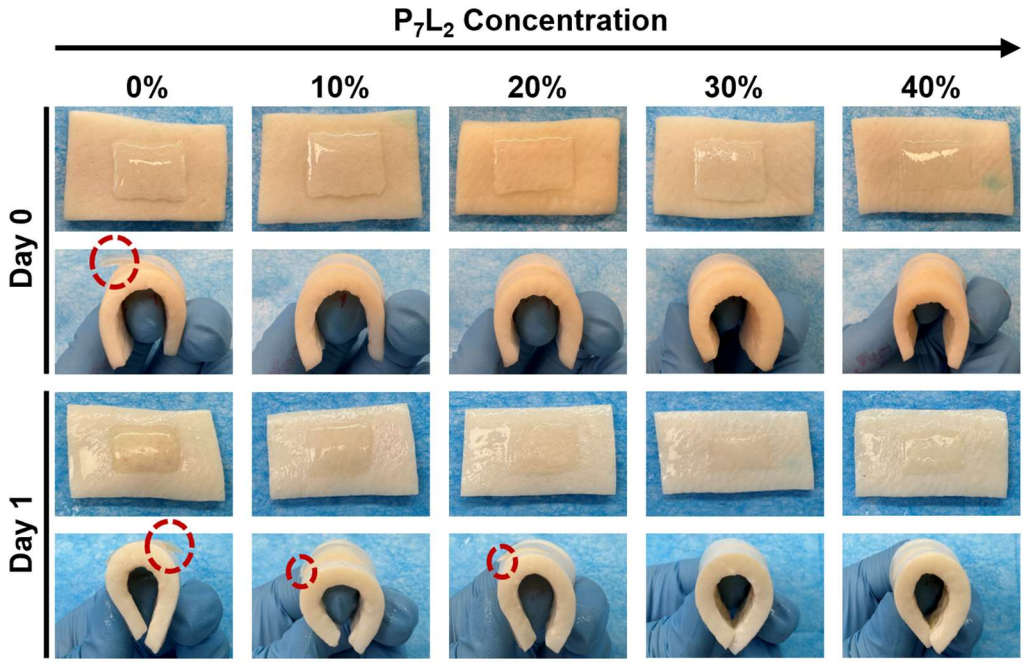

Figure 4-8. Adhesion behaviour of the *in situ*-formed PLD-PS on porcine skin before and after soaking in PBS for 24 hours. The red circles highlight areas where the PLD-PS materials detached from the porcine skins after bending, attributed to the weak adhesion and mismatched mechanical properties.

Finally, burst pressure was evaluated for PLD-PS with different P_7L_2 concentrations on PDMS and porcine skin under both dry and wet conditions. As shown in **Figure 4-9**A, all groups exhibited superior burst pressure exceeding human arterial blood pressure (~ 130 mmHg) [88], with the 30% P_7L_2 group achieving the highest burst pressure (~1500 mmHg, nearly ten times of human arterial blood pressure). Similar results were observed on porcine skin (**Figure 4-9**B). Burst pressure increased with higher P_7L_2 concentrations, peaking at 682.55 ± 130.13 mmHg in the 30% P_7L_2 group.

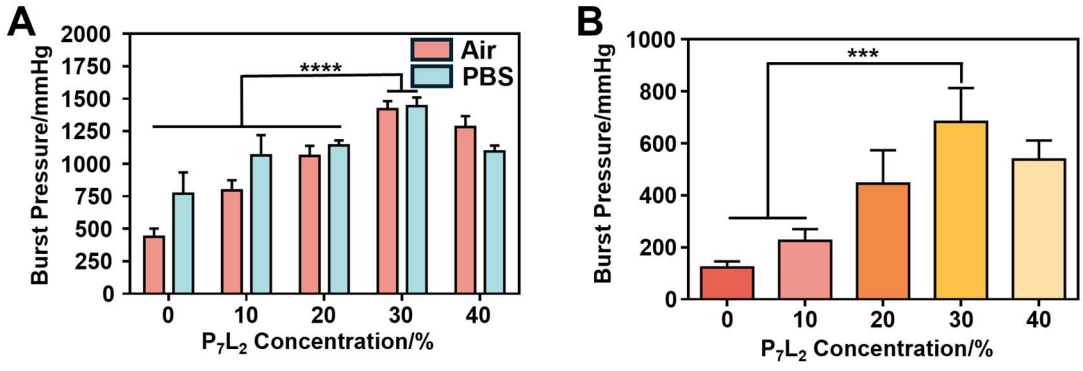

Figure 4-9. Burst pressure of PLD-PS on (A) PDMS and (B) porcine skin.

In conclusion, these experiments systematically evaluated the mechanical and adhesive properties of PLD-PS materials with varying P_7L_2 concentrations. The 30% P_7L_2 group demonstrated the most favourable results. Therefore, the PLD to P_7L_2 ratio for this group was designated as PLD-P, and was fixed for subsequent PTM optimization experiments. Unless otherwise specified, all references to PLD-P in the following sections pertain to this optimal group.

4.3 Optimization of PTM concentration

PTM has the potential to modify the mechanical properties of PLD-PS by forming hydrogen bonds with P_7L_2 and to provide long-term, robust tissue adhesion through the formation of disulfide bonds with tissue. Consequently, PTM optimization was performed by systematically evaluating mechanical properties, adhesive properties, and burst pressure tolerance.

4.3.1 Mechanical properties

Figure 4-10 presents the macroscopic images of PLD-PS with different PTM concentrations under applied compressive force. At 0% PTM, the material behaved as

a hard, rigid solid. As PTM concentration increased, PLD-PS gradually became softer, with the 40% PTM group being fully compressible and exhibiting the greatest softness. After compressive force removal, all groups restored their original shapes, exhibiting excellent elasticity. To quantify these observations, the mechanical properties of PLD-PS were assessed.

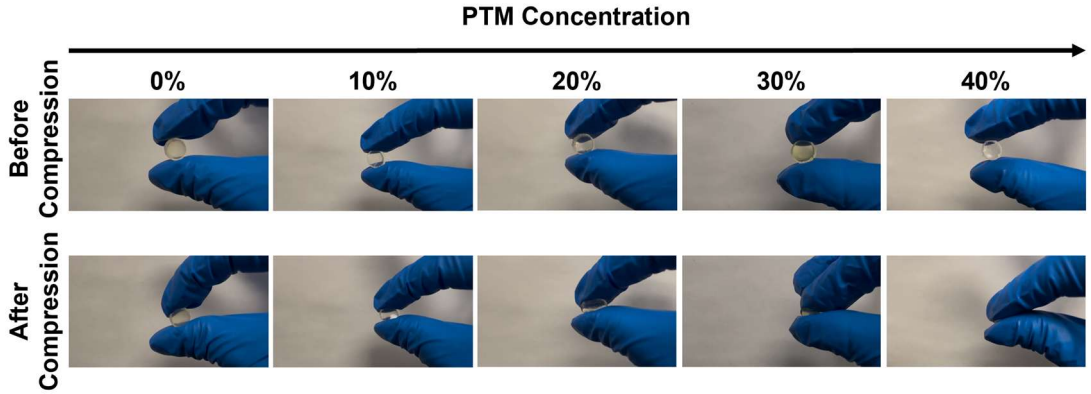

Figure 4-10. Images of PLD-PS with different PTM concentrations under compression.

Tensile testing was conducted to evaluate the effect of PTM on mechanical properties. PLD-PS samples with different PTM concentrations were prepared for the following tensile tests. As shown in **Figure 4-11**, all formulations demonstrated notable elasticity, with the mechanical modulus decreasing from 9.637 ± 0.260 MPa (0% PTM) to 0.200 ± 0.073 MPa (40% PTM). The fracture stress decreased from 1.904 ± 0.429 MPa (0% PTM) to 0.063 ± 0.024 kPa (40% PTM), while the elongation at break increased from 19.304 ± 4.230 (0% PTM) to 32.169 ± 9.848 (40% PTM) (**Table 4-2**). However, the elongation at break did not decrease steadily. This may be attributed to the initial addition of the four-armed PTM, where the introduction of flexible chains enhanced the slip capacity of molecular chains, resulting in increased elongation at break in the 10% PTM group. As PTM content increased further, more hydrogen bonds were introduced into the material system, and the resulting rigid interchain hydrogen bonds limited chain

dissociation, thereby reducing the elongation at break [89]. Finally, at 40% PTM, the flexible chains dominated the material system, allowing easier chain segment movement and improved ductility, leading to the significant increase in elongation at break. Thus, the mechanical properties of PLD-PS can be adjusted by PTM concentration, enabling compatibility with various tissues and organs. The formation of hydrogen bonds between P_7L_2 and PTM increased inter-chain friction and energy dissipation, while higher PTM concentrations resulted in more hydrogen bonds and weaker mechanical properties. This promoted the formation of conformal interfaces between electrodes and tissues, thereby facilitating the precision of physiological signal detection.

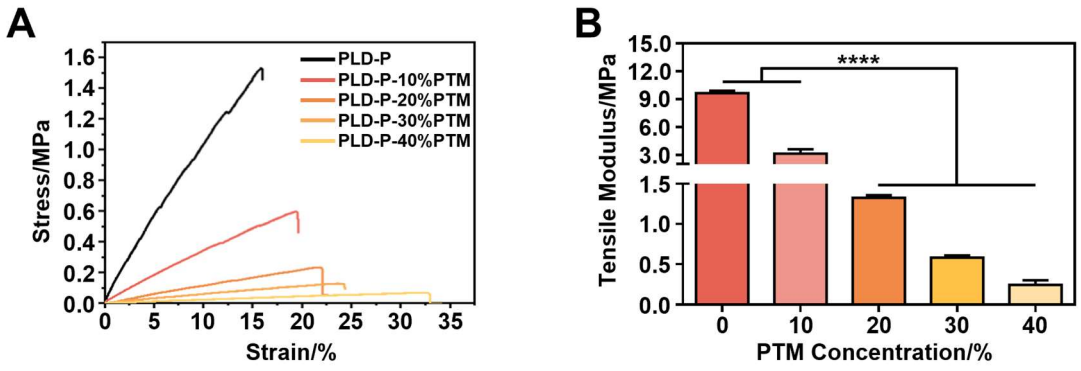

Figure 4-11. Tensile properties of PLD-PS with increasing PTM concentration. (A) The stress-strain curve, and (B) the tensile modulus.

Table 4-2. Tensile mechanical properties of PLD-PS with different PTM concentrations.

Materials	Modulus/MPa	Fracture Stress/MPa	Fracture Strain/%
PLD-P	9.637 ± 0.260	1.904 ± 0.429	19.304 ± 4.230
PLD-P-10%PTM	3.113 ± 0.391	0.679 ± 0.108	21.439 ± 1.638

PLD-P-20%PTM	**1.274 ± 0.097**	**0.233 ± 0.064**	**18.706 ± 4.950**
PLD-P-30%PTM	**0.562 ± 0.034**	**0.092 ± 0.029**	**17.304 ± 5.272**
PLD-P-40%PTM	**0.200 ± 0.073**	**0.063 ± 0.024**	**32.169 ± 9.848**

When PLD-PS is applied to the skin, it experiences compressive forces in addition to tensile forces due to body movement. Therefore, the compressive properties of PLD-PS with different PTM concentrations were also evaluated (**Figure 4-12**). The compressive modulus decreased from 6.920 ± 0.740 MPa (10% PTM) to 0.753 ± 0.084 (40% PTM), which is significantly lower than that of PLD-P (433.425 ± 69.744 MPa) (**Table 4-3**). This phenomenon is attributed to the incorporation of flexible PTM. Notably, the compressive modulus of PLD-PS is comparable to that of natural skin. In summary, PLD-PS with adjustable and suitable mechanical properties was successfully fabricated.

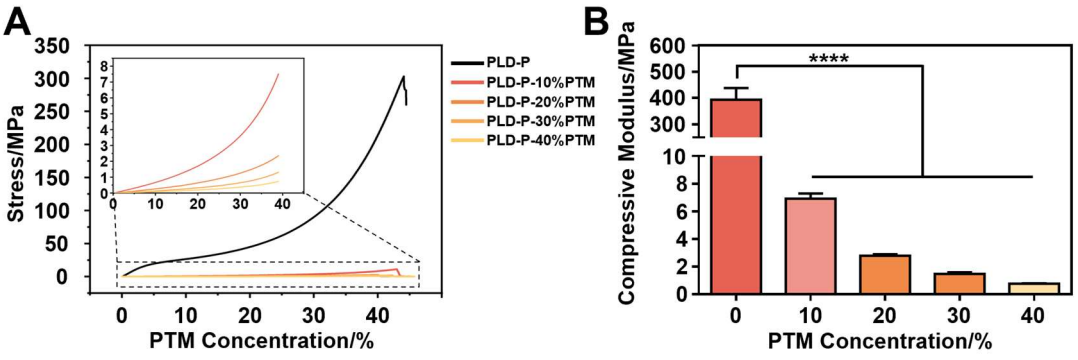

Figure 4-12. Compressive properties of PLD-PS with increasing PTM concentration. (A) The stress-strain curve, and (B) the compressive modulus.

Table 4-3. Compressive mechanical properties of PLD-PS with different PTM

concentrations.

Materials	Modulus/MPa	Fracture Stress/MPa	Fracture Strain/%
PLD-P	**433.425 ± 69.744**	**303.990 ± 23.699**	**46.145 ± 2.164**
PLD-P-10%PTM	**6.920 ± 0.740**	**7.913 ± 2.176**	**38.833 ± 3.005**
PLD-P-20%PTM	**2.783 ± 0.222**	**2.761 ± 0.905**	**42.665 ± 3.674**
PLD-P-30%PTM	**1.468 ± 0.241**	**1.265 ± 0.361**	**39.793 ± 6.314**
PLD-P-40%PTM	**0.753 ± 0.084**	**0.928 ± 0.233**	**44.118 ± 2.506**

4.3.2 Adhesive properties

When in contact with skin, PLD-PS rapidly formed instantaneous adhesion through hydrogen bonding, followed by the gradual formation of strong covalent disulfide bonds between the material and the skin, ensuring long-lasting and stable adhesion. To quantify adhesive strength, the *in situ*-formed PLD-PS was tested on porcine skin through the lap-shear method. For this evaluation, the side of the adhesive not in contact with porcine skin was fixed to another porcine skin using commercial glue, ensuring that the measured value reflected the adhesive strength of PLD-PS. As shown in **Figure 4-13**A, adhesive strength remained relatively low (less than 20 kPa) at lower PTM concentration and increased gradually, reaching a maximum of approximately 60 kPa at 40% PTM. Additionally, the interfacial toughness of PLD-PS after crosslinking was measured by the 180º peeling test. Similarly, the side of PLD-PS not in contact with porcine skin was fixed to another piece of porcine skin with commercial glue to ensure accurate measurement of interfacial toughness. As shown in **Figure 4-13**B, increasing PTM concentration led to a significant enhancement in interfacial toughness, rising

approximately ten-fold from ~37.5 J/m^2 (0% PTM) to ~459 J/m^2 (40% PTM). These findings demonstrated the excellent adhesive properties of PLD-PS on porcine skin, which were essential for conformal adhesion, effective tissue sealing, and improved sensing accuracy.

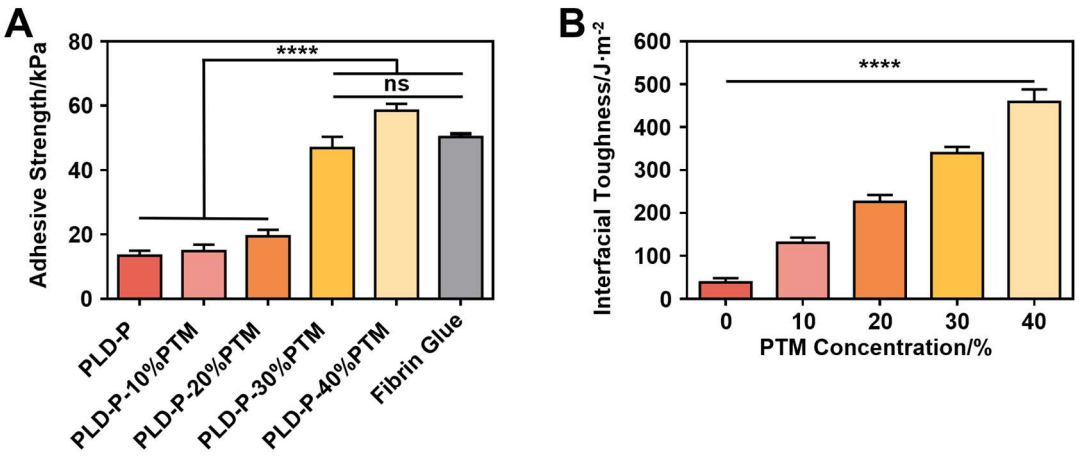

Figure 4-13. The (A) adhesive strength and (B) interfacial toughness of PLD-PS with different PTM concentrations on porcine skin.

However, hydrogen bonds formed between the adhesive material and the tissue could be easily disrupted in the presence of water [90], resulting in reduced transient adhesion and potentially affecting subsequent disulfide bond formation. Therefore, the adhesive strength of PLD-PS was evaluated after immersion in water. Adhesion to porcine skin was assessed on day 0 and after soaking in PBS for one day. As shown in **Figure 4-14**A, only the 30% PTM and 40% PTM groups adhered firmly to porcine skin on day 0, other groups failed due to mismatched mechanical properties and insufficient adhesion. After soaking in PBS for one day, only the 30% PTM and 40% PTM maintained adhesion to porcine skin. The tissue adhesion provided by PTM resulted from the formation of disulfide (S-S) bonds with tissues, which were typically resistant

to breakage under physiological conditions, ensuring robust adhesion. Adhesive strength measurements after soaking (**Figure 4-14**B) showed a similar trend, confirming the superior water-resistant adhesive properties of the 30% PTM and 40% PTM groups.

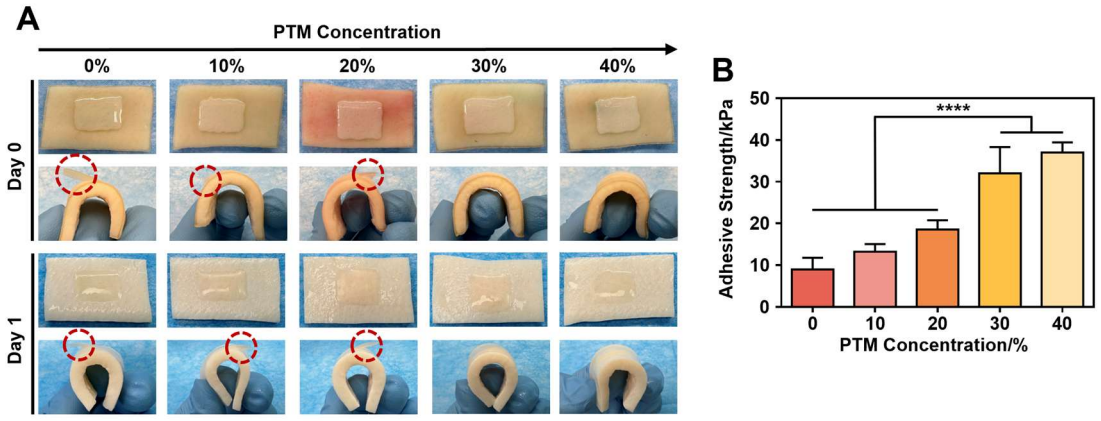

Figure 4-14. (A) Images of the adhesion behaviour of the *in situ*-formed PLD-PS with different PTM concentrations adhering to the porcine skin before and after soaking in PBS for 24 hours. The red circles highlight areas where the PLD-PS materials detached from the porcine skins after bending, attributed to the weak adhesion and mismatched mechanical properties. (B) Adhesive strength of PLD-PS with different PTM concentrations on porcine skin after soaking in PBS for one day.

4.3.3 Burst pressure tolerance

To assess pressure tolerance, burst pressure was measured on both PDMS and porcine skin. PDMS served as the substrate for assessing the burst pressure tolerance of PLD-PS against commonly used engineering solids. Both air and PBS were pumped out to test pressure tolerance under dry and wet conditions. **Figure 4-15**Ai shows that nearly all groups exhibited burst pressures exceeding 1000 mmHg, far surpassing human arterial blood pressure (~ 130 mmHg) in both conditions, due to the formation of

mechanical interlocks (**Figure 4-15**Aii&Aiii). Porcine skin was also used to mimic human skin function, and PLD-PS demonstrated enhanced anti-leakage properties, with the highest (495.04 ± 68.47 mmHg) observed in the 30% PTM group (**Figure 4-15**B).

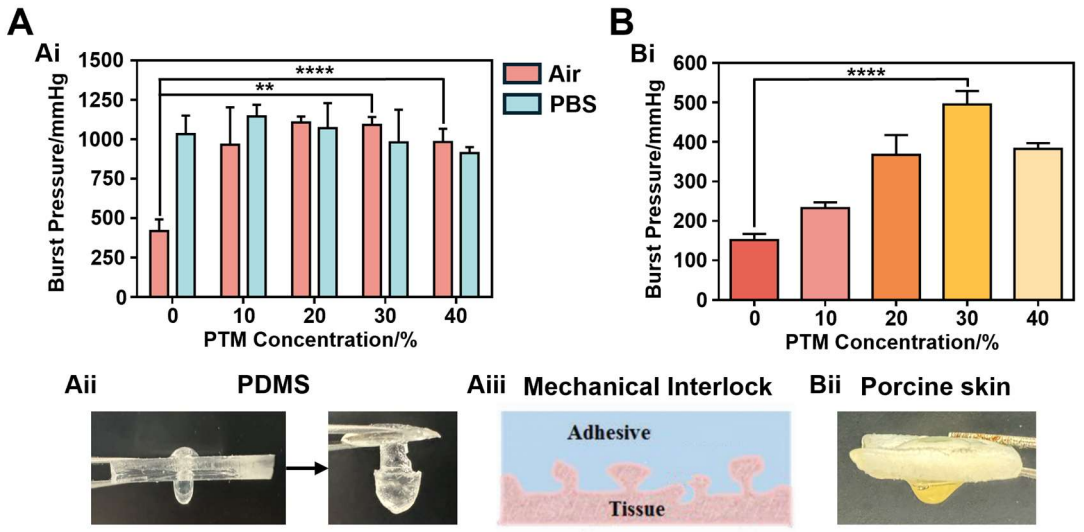

Figure 4-15. Burst pressure of PLD-PS on (Ai) PDMS and (Bi) porcine skin. (Aii) The plug-shaped PLD-PS formed *in situ* on PDMS during application. (Aiii) Schematic diagram of the mechanical interlock formed between adhesives and tissues. (Bii) The plug-shaped PLD-PS formed *in situ* on the porcine skin.

Notably, compared with commercial adhesive products (such as fibrin glue and cyanoacrylate) and recently reported adhesive materials [21], PLD-PS exhibited significantly higher burst pressure (**Figure 4-16**).

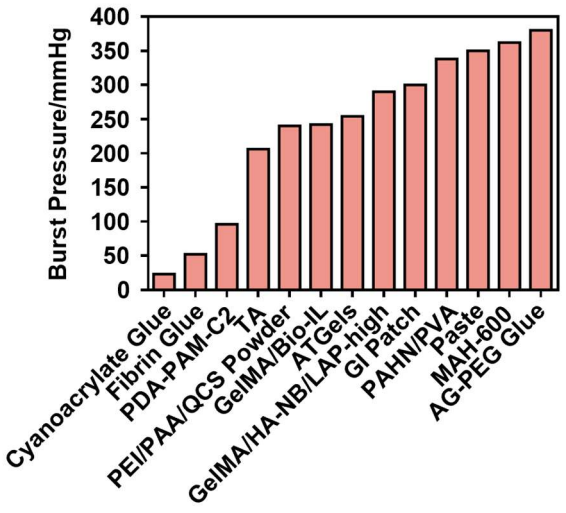

Figure 4-16. Burst pressure of some recently reported adhesive materials.

In summary, the 40% PTM group exhibited soft mechanical properties and reliable adhesion performance, making it the optimal choice for subsequent experiments. Unless otherwise specified, all subsequent references to PLD-PS refer to the 40% PTM group.

4.4 Physical properties

4.4.1 Swelling

Current adhesives tend to swell in aqueous environments, which adversely affects their applications (including their mechanical properties, adhesive properties, and *in vivo* biocompatibility). Previous studies have reported that swollen materials exhibit reduced mechanical properties, resulting in strain mismatch between the material and tissue, thereby further weakening adhesion [21]. Additionally, swelling has been shown to induce severe chronic inflammatory responses in rat subcutaneous muscle [22]. Therefore, we evaluated the swelling properties of PLD-PS in PBS, where the volume increase of PLD-PS was barely visible over 120 h (**Figure 4-17**). As shown in **Figure**

4-18A, PLD-PS exhibited a limited swelling ratio (~ 2%) over five days. This minimal swelling was attributed to the tight covalent crosslinking network and the abundance of hydrophobic groups in PLD-PS, which restricted water penetration. To further evaluate the impact of swelling on mechanical properties, we conducted tensile tests after immersion for seven days. The results showed that swelling had no significant effect on the mechanical properties of PLD-PS (**Figure 4-18**B). These findings confirm the low swelling property of PLD-PS, supporting its potential for long-term stable application.

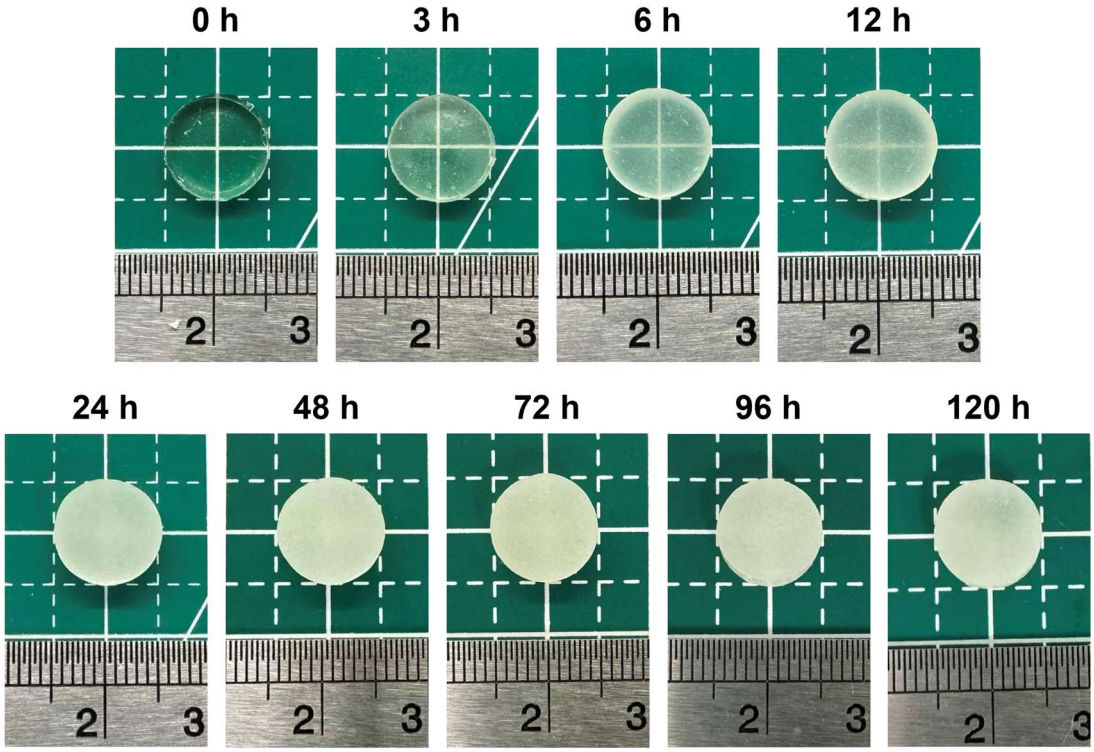

Figure 4-17. Swelling exhibition of PLD-PS before and after immersion in PBS for 120 hours.

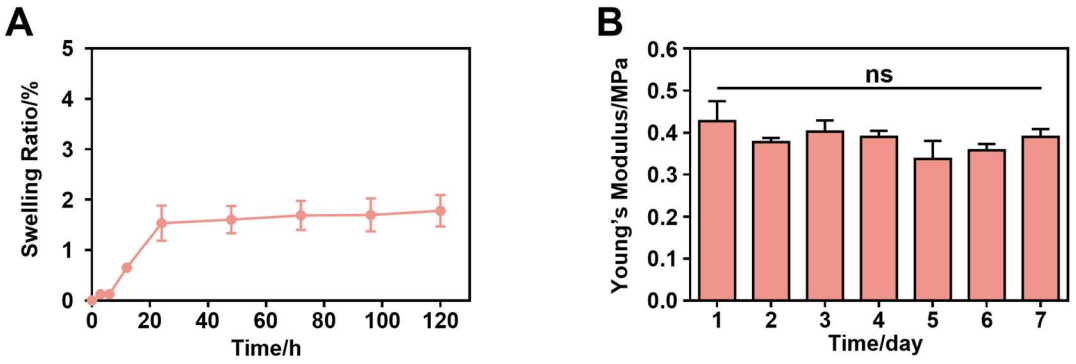

Figure 4-18. Swelling properties of PLD-PS. (A) Swelling ratio of PLD-PS with a function of time. (B) Mechanical properties of PLD-PS after swelling.

4.4.2 Water contact angle (WCA)

The hydrophilicity significantly influences both the adhesive and swelling properties of the materials. Therefore, we evaluated the hydrophilicity of PLD, PLD-P and PLD-PS using water contact angle measurements. As indicated in **Figure 4-19**, PLD exhibited the largest WCA, indicating hydrophobicity. Further incorporation of P_7L_2 turned PLD-P into a hydrophilic material by introducing hydrogen bonds, resulting in a decreased WCA. Conversely, the addition of PTM, as a hydrophobic group, to PLD-P significantly increased the hydrophobicity of the material. The existence of a hydration layer at the interface can impede effective interactions between the adhesive and the substrate, resulting in a sharp reduction in adhesion performance. In contrast, the hydrophobic properties of PLD-PS facilitate drainage, helping to eliminate the hydrated water at the adhesion interface and thereby enhancing the material's adhesion to the skin.

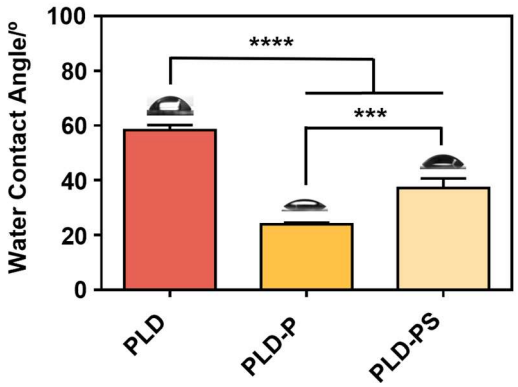

Figure 4-19. Water contact angles of PLD, PLD-P and PLD-PS.

4.4.3 Water vapor transmission rate (WVTR)

It was reported that the human body will insensibly lose water in the form of moisture vapor from the skin at an average evaporation rate of 23–28 g/hour·mm^2 for thermoregulation under the rest condition, where hands and soles exhibited a relatively higher perspiration rate of >30 g/hour·mm^2 [91], while this rate will be enhanced during exercise. Thus, the breathability is of great importance for the wearability of the sensors. What's more, for the traditional hydrogel-based flexible sensors, water evaporation may lead to dehydration, structural collapse and shrinkage, which challengingly limit the long-term application of those sensors and impact their electronic sensing performance [92]. Therefore, the controlled permeable capacity was quantified through the water vapor transmission rate (WVTR) (**Figure 4-20**). It was found that the widely utilized flexible substrate PDMS and our PLD group presented markedly decreased permeability, with the WVTR of ~5 g/hour·mm^2 and ~36 g/hour·mm^2, respectively, due to their high-density microstructure and high hydrophobicity, which may hinder the evaporation of sweat from the skin and lead to inflammation after long-term wearing [93]. On the other hand, the PLD-P formed a relatively weak crosslink network and exhibited hydrophilicity, showing WVTR of ~70 g/hour·mm^2, which may cause fast water erosion to the sensing layer and reduce the service life of the flexible sensor [94].

Encouragingly, we observed that the PLD-PS exhibited a moderate WVTR of ~45 g/hour·mm^2, which could be attributed to the formation of the covalent crosslink network. This moderate WVTR value helps to balance the skin comfort and sensing layer protection of a wearable flexible sensor.

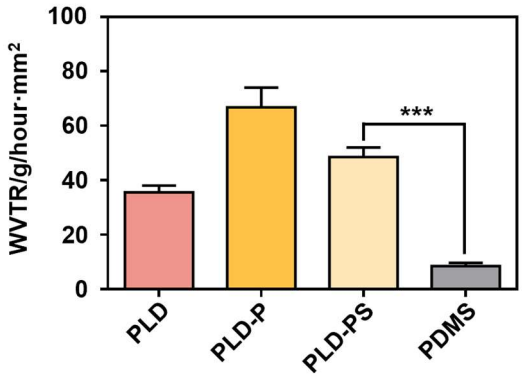

Figure 4-20. Water vapor transmission rate of PLD, PLD-P, PLD-PS and a widely used flexible substrate PDMS.

4.4.4 Degradation

We also evaluated the degradation rates of PLD, PLD-P, and PLD-PS in deionized water (ddH_2O). As shown in **Figure 4-21**, all three groups demonstrated slow degradation, with less than ~25% mass loss over 21 days. PLD possessed a tight cross-linked network and exhibited the slowest degradation rate (~ 3% mass loss). After doping with P_7L_2, the crosslinked network of PLD-P was dispersed, as P_7L_2 could not form covalent crosslinks with P_7L_2DMA due to the absence of carbon-carbon double bonds. Instead, P_7L_2 depended on non-covalent interactions, including hydrogen bonds and van der Waals forces, which were weakened upon immersion in water, resulting in unstable crosslinks and the fastest degradation rate among the three materials. Further incorporation of PTM into PLD-P enables the tetra-armed thiol PTM to form covalent

crosslinks with P_7L_2DMA via Michael addition, confining free P_7L_2 within the crosslinked network of PLD-PS. However, the non-covalent interactions between PTM and P_7L_2 remain weak, resulting in a moderate degradation rate of PLD-PS.

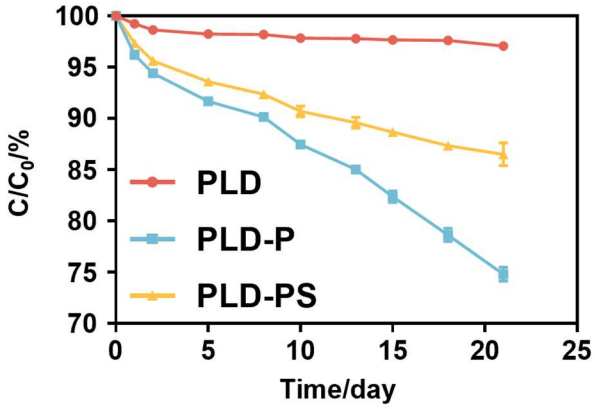

Figure 4-21. Degradation of PLD-PS in ddH_2O for 21 days.

4.5 Biocompatibility

4.5.1 Cytocompatibility

While outstanding mechanical strength and adhesion are crucial characteristics for adhesives, biocompatibility remains a fundamental requirement for their *in vivo* applications. After optimizing the concentrations of P_7L_2 and PTM, we evaluated the biocompatibility of P_7L_2DMA, PLD-P, and PLD-PS by culturing L929 cells with material extracts, while the commercial product cyanoacrylate glue (COMPONT®) was utilized as a control. In the live/dead assay, all materials demonstrated cytocompatibility similar to that of the control medium, with no observable dead cells after one and three days of culture (**Figure 4-22**A). All groups still maintained over 95% viability after three days of incubation (**Figure 4-22**B). However, cyanoacrylate glue exhibited cytotoxicity of ~91% viability in three days, which is attributed to the rapid degradation into cyanoacetate and formaldehyde [95].

Cell proliferation was further assessed using the CCK-8 assay after one and three days of incubation (**Figure 4-22**C). The sustained and stable increase in cell growth indicated that none of the materials had a detrimental effect on cell proliferation, while the cyanoacrylate glue presented inhibited proliferation as its degradation products induced acute and chronic inflammation [96]. These results confirmed the good cytocompatibility of our PLD-PS material, demonstrating its potential for biomedical applications.

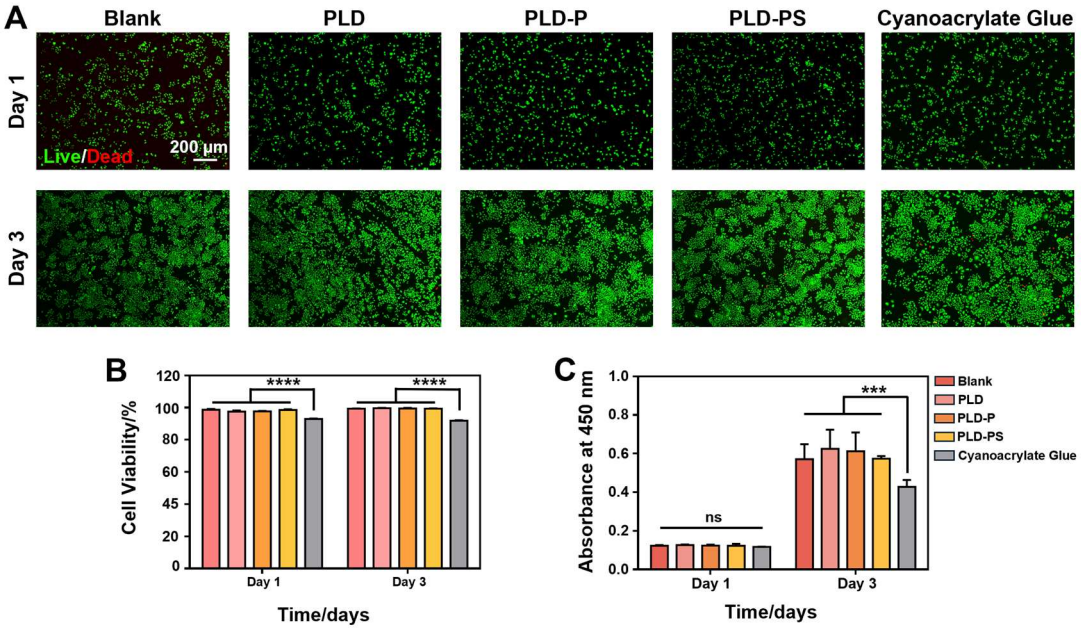

Figure 4-22. *In vitro* biocompatibility of PLD, PLD-P, and PLD-PS after 1 and 3 days of culture. (A) Live & dead staining, (B) cell viability and (C) cell proliferation.

4.5.2 Hemocompatibility

An *in vitro* haemolysis test was conducted to evaluate the hemocompatibility of PLD-PS, using PBS as the negative control and Triton X-100 as the positive control. As shown in **Figure 4-23**A, all three material groups appeared clear and transparent,

similar to the negative control group, whereas the positive control group exhibited a red coloration. Quantitative analysis of the supernatants (**Figure 4-23**B) showed that the haemolysis ratio for all samples was below 1%, well within the ISO 10993-5 safety threshold of 5%, indicating excellent hemocompatibility.

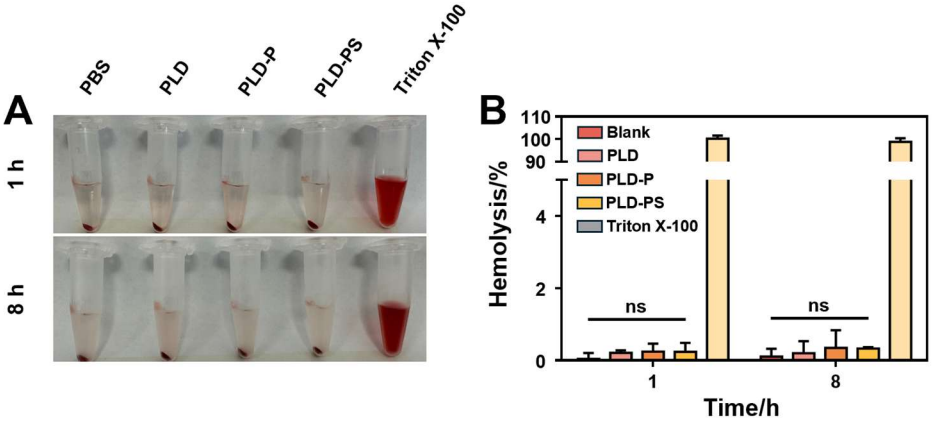

Figure 4-23. *In vitro* hemocompatibility of PLD-PS. (A) Images of haemolysis and (B) haemolysis ratio after 1 and 8 hours of incubation.

4.6 Sealing of different organs

In addition to the application as a skin tissue adhesive, our PLD-PS was also approved to be successfully utilized for various tissue sealing. To demonstrate the biological adhesion properties of PLD-PS on various organs, we applied the material as a tissue sealant to the intestine, kidney, and liver. As shown in **Figure 4-24**, PLD-PS achieved secure adherence to these organs, with the capacity to flexibly conform to dynamic tissues. For liquid sealing efficiency, PLD-PS effectively sealed the needle-punctured hole and prevented liquid leakage from perforated, liquid-filled porcine intestine under high pressure. For tissue closure, PLD-PS provided tight sealing of the severed kidney and liver. These results suggested the diverse tissue adhesion capacity and adaptability of PLD-PS.

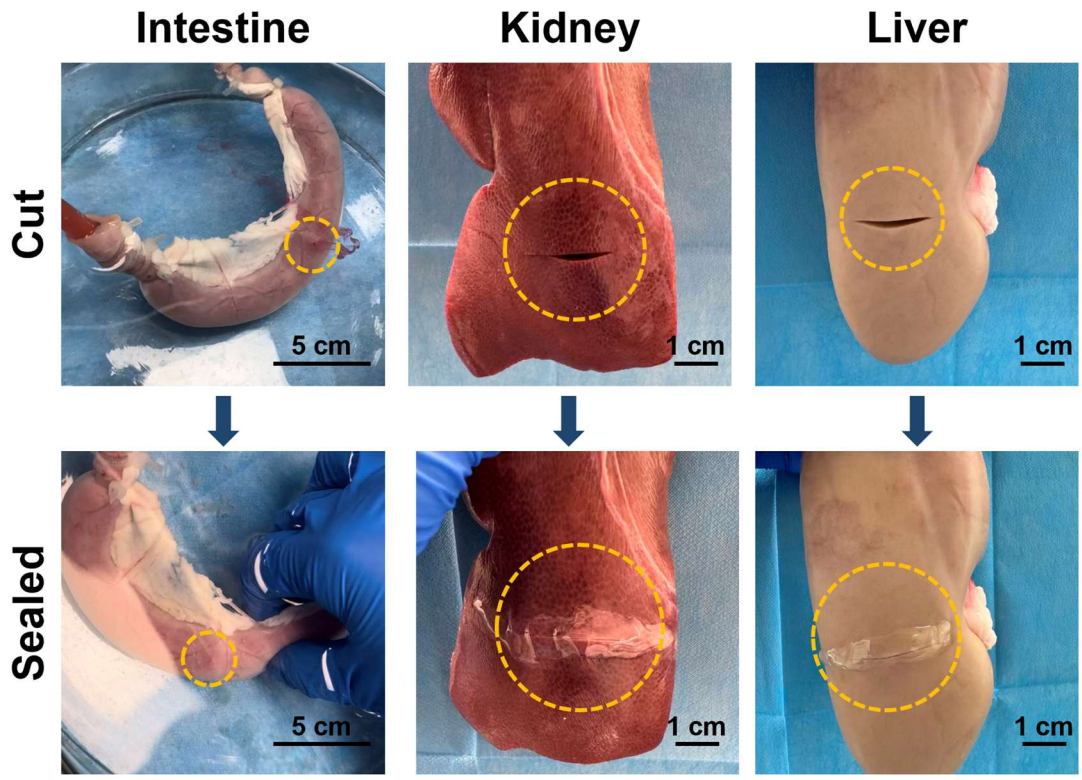

Figure 4-24. Sealing performance of PLD-PS on kidney, intestine and liver.

4.7 Sensing properties

Finally, we evaluated the sensing performance of the PLD-PS-based sensor under different strains (**Figure 4-25**). The samples demonstrated a broad sensing range (from 0 to over 100% strain). Sensitivity was quantified using the gauge factor (GF), where higher GF values correspond to enhanced sensitivity, which is an important attribute for the precise detection of localized physiological signals, such as pulses. The result showed that the GF of the sensor increased with strain, and eventually reached 2.38.

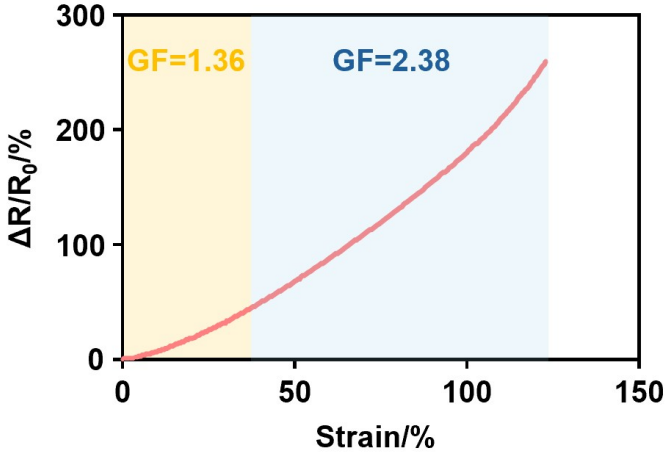

Figure 4-25. Relative resistance and relative GF changes as a function of tensile strain.

The stability of the PLD-PS-based sensor was further evaluated by monitoring resistance changes under cyclic stretch. As shown in **Figure 4-26**, over ten cycles, the resistance consistently increased when the sensor was stretched and decreased upon release. However, after every single cycle, the resistance did not fully recover to its initial value, instead exhibiting a gradual upward trend, with an overall increase of 37.9% after ten cycles. This phenomenon is attributed to the high surface tension of the liquid metal Ga-In [58], which shows a tendency to cohesion during stretching, resulting in cracks in the stretched circuit and a consequent rise in resistance (**Figure 4-27**). To address this issue, a sandwich-structured sensing patch was developed, in which the Ga-In circuit layer was encapsulated within the middle of the structure. This design prevents circuit breakage and liquid metal leakage, thereby enhancing sensing stability. By geometrically confining and guiding the extension of the Ga-In layer, this approach addresses the defects and cracks caused by the high surface tension of the liquid metal, ultimately enabling long-term and stable sensor performance.

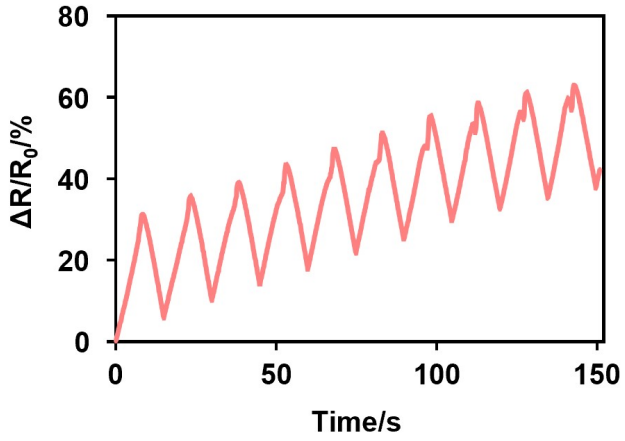

Figure 4-26. Relative resistance changes of PLD-PS-based sensor at 10% strain.

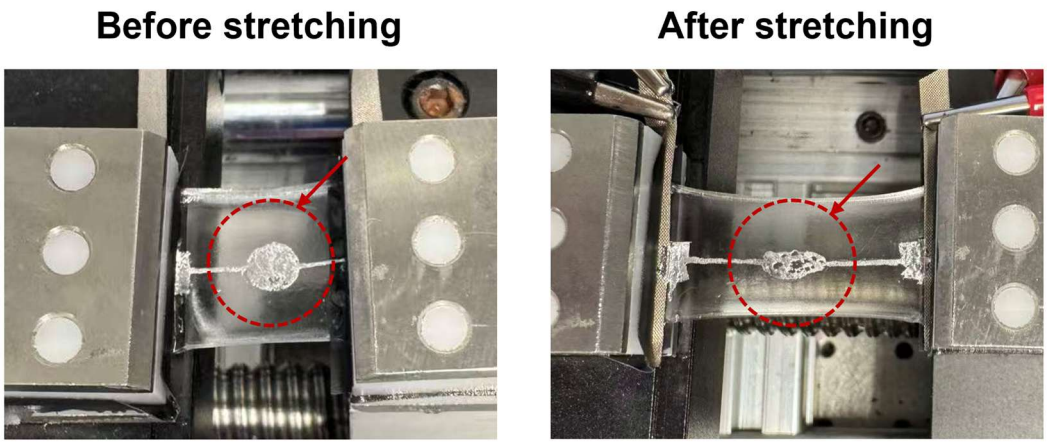

Figure 4-27. Cracking performance of Ga-In during the stretch process.

Figure 4-28 presents the relative resistance changes of the sandwich-structured PLD-PS-based sensor under cyclic strains of 5%, 10%, 15% and 20%, respectively. The electrical signals generated at different strains exhibited clear distinctions, with a direction proportionality between the maximum $\Delta R/R_0$ and the applied strain. What's more, the sensor demonstrated stable and highly reproducible sensing performance throughout the tests, indicating that the sandwich-structured design effectively

enhances both the stability and durability of the sensor.

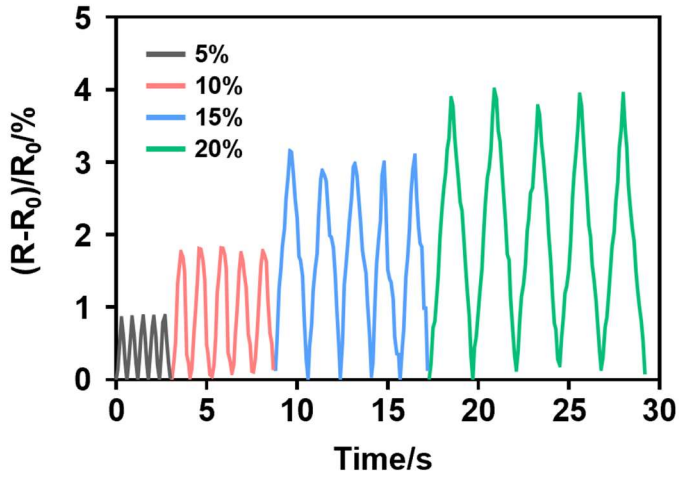

Figure 4-28. Changes in the relative resistance of the PLD-PS-based sensor under 5%, 10%, 15% and 20% dynamic stretch.

After that, the PLD-PS-based sensor was immersed in PBS and soaked for 1 day. The relative resistance during cyclic stretch after immersion (**Figure 4-29**) presented consistent, stable, and repetitive signals compared to **Figure 4-28**. This remarkable retention of the electronic sensing performance in the prolonged aqueous environment is attributed to the superior anti-swelling and low degradation properties of our material. Furthermore, the confined sandwich structure effectively minimized the fluid erosion and stabilized the conductive functional layer. This result confirmed the potential for reliable long-term practical applications.

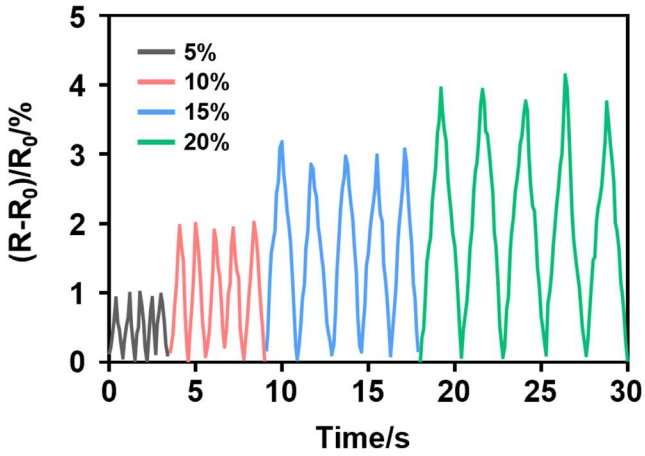

Figure 4-29. Relative resistance signals of the PLD-PS-based sensor under 5%, 10%, 15% and 20% dynamic stretch after immersing in PBS for one day.

Subsequently, the sensor was attached to different parts of the human body, including the wrist, elbow, and finger, where the signal generated by body movement was recorded. As shown in **Figure 4-30,** the electrical signals obtained from different parts of the human body reflect differences in diverse human activities, and the sensing signals exhibited high repeatability and stability throughout the measurements.

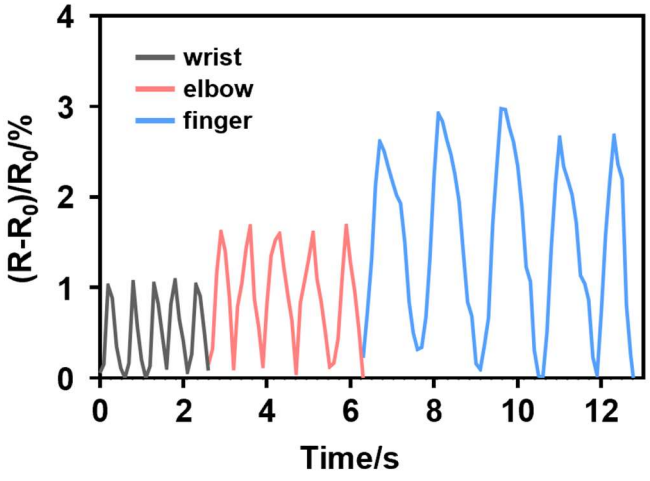

Figure 4-30. Relative resistance of the PLD-PS sensor during movement in the wrist, elbow, and finger.

Moreover, by integrating Morse code, the PLD-PS sensors are capable of transmitting various alphanumeric messages, such as "SOS" (**Figure 4-31**A) and "HELLO" (**Figure 4-31**B).

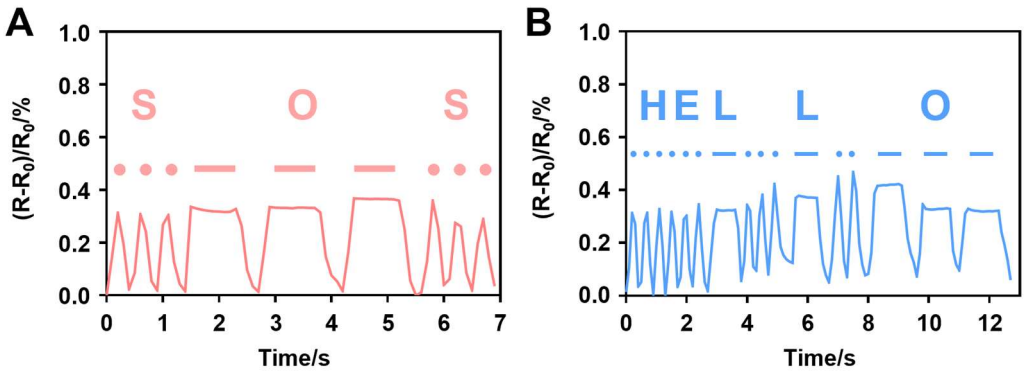

Figure 4-31. The PLD-PS-based sensor outputs the letters (A) "SOS" and (B) "HELLO" of Morse code.

These results demonstrate that the sandwich-structured PLD-PS-based sensor exhibits excellent responsiveness, repeatability, and stability. The sensor is capable of both monitoring human joint movements and transmitting Morse code information. Consequently, the PLD-PS-based sensor shows potential for the detection of human biological signals.

5. Conclusions and recommendations for future work

5.1 Major findings and conclusions

In this study, we developed a soft, elastic, and adhesive bandage called PLD-PS, fabricated by simply mixing crosslinkable P_7L_2DMA, P_7L_2, and PTM. This bandage featured tuneable mechanical properties and anti-swelling properties for use as a tissue sealant and in human physiological signal detection. Initially, we synthesized two P_mL_nDMA materials with different m and n concentrations (P_7L_2DMA and $P_{68}L_8$DMA), and evaluated their mechanical properties. By comparing these mechanical properties with those of various tissues, we finally selected P_7L_2DMA as the framework for PLD-PS.

Subsequently, we optimized the concentrations of P_7L_2 and PTM by assessing the mechanical and adhesive properties of PLD-PS. The mechanical properties of PLD-PS were tuneable, with Young's modulus ranging from approximately 10 MPa to 100 kPa, by adjusting P_7L_2 and PTM concentration, and meanwhile exhibiting elasticity, making it suitable for both hard and soft tissues. Regarding adhesive properties, PLD-PS exhibited robust adhesion to porcine skin, surpassing that of the widely used commercial product fibrin glue, and maintained adhesion even after immersion in PBS, indicating its potential for tight and conformal adhesion. The anti-leakage properties of PLD-PS were also evaluated on PDMS and porcine skin under both dry and wet conditions. PLD-PS was shown to withstand extremely high burst pressure (about 6.7 times greater than human arterial blood pressure) by forming a mechanical interlock to prevent leakage. We further assessed the anti-swelling properties (less than 2% over 5 days, with no impact on mechanical properties) and degradation properties (less than 15% over 21 days), confirming the long-term stability of PLD-PS. Haemostatic performance was also tested. Although PTM incorporation accelerated haemostasis compared to the non-PTM group, PLD-PS did not outperform the commercial

haemostatic material. Additionally, the biocompatibility of PLD-PS, including cytocompatibility and hemocompatibility, was also evaluated. PLD-PS demonstrated good cytocompatibility compared with the commercial cyanoacrylate glue (COMPONT®), with sustained cell growth after three days of incubation, and excellent hemocompatibility, with a very low haemolysis ratio after eight hours of direct contact. We then applied PLD-PS to various organs, where it showed effective liquid sealing and tissue closure, confirming its highly conformal adhesion to various of dynamic tissues. Finally, we fabricated conductive patterns using liquid metal on the surface of the PLD-PS bandage and evaluated the sensing performance of the PLD-PS-based sensor under different and cyclic strains, and compared the sensing performance after one day of immersion in wet environments. We also successfully applied the sensor to various joints for the detection of body movements and transmitting Morse code signals.

Given these advantages, we believe that PLD-PS has significant potential to serve as a novel adhesive bandage for sutureless tissue repair and accurate human physiological signal monitoring.

5.2 Recommendations for future work

In this project, we developed a novel soft, elastic, and adhesive bandage, PLD-PS, for wound closure and human physiological signals detection. However, certain limitations remain in both applications that require further optimization and improvement.

For wound closure applications, although we achieved tuneable mechanical properties, the current system still exhibited brittleness, with a maximum strain tolerance of no more than 40% during tensile testing. Therefore, further research should focus on enhancing the toughness of PLD-PS. Furthermore, the elasticity of PLD-PS needs to be

quantified by cyclic tensile tests. Additionally, while PLD-PS demonstrated superior adhesive properties compared to commercially available products in porcine skin, its instantaneous adhesion relied on hydrogen bonding, which was significantly weakened by water molecules, resulting in a reduced underwater adhesion. What's more, the burst pressure of the pre-formed adhesive PLS-PS patches was also needed, to evaluate the sealing performance of the sensing patch. Therefore, future work will also improve the wet adhesion properties of PLD-PS to broaden its application scope. Furthermore, our work has progressed only to the cellular experimentation stage. Subsequent plans will involve subcutaneous implantation of PLD-PS in rats to assess the inflammatory response post-implantation and evaluate *in vivo* biocompatibility.

For human physiological signal detection, current circuit fabrication processes remain immature, resulting in relatively low sensing sensitivity (GF). Subsequently, we will further optimize the circuit fabrication process, trying to fabricate more complex and practical circuits. Additionally, the present study has only tested the electrical resistance of the material under different strain conditions *in vitro* and for only one day, without yet assessing human psychological signals (such as ECG, pulse, etc.), as well as long-term sensing performances. To address this limitation and systematically advance this work, the following experimental investigations will be involved, including but not limited to the evaluation of repeatable sensing performance under hundreds of cyclic tensile in long-term applications, the consistency of resistance response, fatigue behaviour, and hysteresis in load-unload curves. What's more, resistance response under combined deformation modes such as bending, torsion, and point loading will also be evaluated to align with real-world applications. Further, we will apply the PLD-PS-based sensor to animal models for *in vivo* collection and monitoring of electrocardiographic signals. We also plan to attach PLD-PS sensors to the human body for pulse signal acquisition and monitoring. By these experiments, we hope to comprehensively assess the realistic sealing and sensing performance of the bandage

under physiological environments, and gain a deep understanding of the sensing signals for reliable application, thereby developing high-performance and highly reliable flexible sensing systems.

References

[1] G. d. Marzo, V. M. Mastronardi, M. T. Todaro, L. Blasi, V. Antonaci, L. Algieri, M. Scaraggi, M. De Vittorio, Sustainable electronic biomaterials for body-compliant devices: challenges and perspectives for wearable bio-mechanical sensors and body energy harvesters, Nano. Energ. 123 (2024) 109336.

[2] C. Lim, Y. J. Hong, J. Jung, Y. Shin, S.-H. Sunwoo, S. Baik, O. K. Park, S. H. Choi, T. Hyeon, J. H. Kim, Tissue-like skin-device interface for wearable bioelectronics by using ultrasoft, mass-permeable, and low-impedance hydrogels, Sci. Adv. 7 (19) (2021) eabd3716.

[3] J. Ubrani, R. Reith, R. T. Llamas. Wearable Devices Market Insights. IDC Corporate, (2024).

[4] S. Guarducci, S. Jayousi, S. Caputo, L. Mucchi, Key fundamentals and examples of sensors for human health: wearable, non-continuous, and non-contact monitoring devices, Sensors 25 (2) (2025) 556.

[5] J. Park, H. W. Kim, S. Lim, H. Yi, Z. Wu, I. G. Kwon, W. H. Yeo, E. Song, K. J. Yu, Conformal fixation strategies and bioadhesives for soft bioelectronics, Adv. Funct. Mater. 34 (22) (2024) 2313728.

[6] H. Jung, H. Lee, M. Shin, D. Son, Adhesive bioelectronics for closed-loop therapy, Med-X 3 (1) (2025) 11.

[7] S. J. Wu, J. Wu, S. J. Kaser, H. Roh, R. D. Shiferaw, H. Yuk, X. Zhao, A 3D printable tissue adhesive, Nat. Commun. 15 (1) (2024) 1215.

[8] Y. Zheng, K. Shariati, M. Ghovvati, S. Vo, N. Origer, T. Imahori, N. Kaneko, N. Annabi, Hemostatic patch with ultra-strengthened mechanical properties for efficient adhesion to wet surfaces, Biomaterials 301 (2023) 122240.

[9] A. K. S. Chandel, A. Shimizu, K. Hasegawa, T. Ito, Advancement of biomaterial-based postoperative adhesion barriers, Macromol. Biosci. 21 (3) (2021) 2000395.

[10] S. B. Dharap, P. Barbaniya, S. Navgale, Incidence and risk factors of postoperative complications in general surgery patients, Cureus 14 (11) (2022) e30975.

[11] H. An, M. Zhang, Z. Huang, Y. Xu, S. Ji, Z. Gu, P. Zhang, Y. Wen, Hydrophobic cross-linked chains regulate high wet tissue adhesion hydrogel with toughness, anti-hydration for dynamic tissue repair, Adv. Mater. 36 (8) (2024) 2310164.

[12] H. Wang, X. Yi, T. Liu, J. Liu, Q. Wu, Y. Ding, Z. Liu, Q. Wang, An integrally formed janus hydrogel for robust wet-tissue adhesive and anti-postoperative adhesion, Adv. Mater. 35 (23) (2023) 2300394.

[13] K. Chen, C. Liu, J. Huang, L. Che, Y. Yuan, C. Liu, A conformable and tough janus adhesive patch with limited 1D swelling behavior for internal bioadhesion, Adv. Funct. Mater. 33 (41) (2023) 2303836.

[14] K. C. Wu, B. R. Freedman, P. S. Kwon, M. Torre, D. O. Kent, W. L. Bi, D. J. Mooney, A tough bioadhesive hydrogel supports sutureless sealing of the dural membrane in porcine and ex vivo human tissue, Sci. Transl. Med. 16 (739) (2024) eadj0616.

[15] P. A. Leggat, D. R. Smith, U. Kedjarune, Surgical applications of cyanoacrylate adhesives: a review of toxicity, ANZ J. Surg. 77 (4) (2007) 209-213.

[16] H. Ren, Z. Zhang, X. Cheng, Z. Zou, X. Chen, C. He, Injectable, self-healing hydrogel adhesives with firm tissue adhesion and on-demand biodegradation for sutureless wound closure, Sci. Adv. 9 (33) (2023) eadh4327.

[17] C. Cui, T. Wu, X. Chen, Y. Liu, Y. Li, Z. Xu, C. Fan, W. Liu, A janus hydrogel wet adhesive for internal tissue repair and anti-postoperative adhesion, Adv. Funct. Mater. 30 (49) (2020) 2005689.

[18] W. Yang, X. Kang, X. Gao, Y. Zhuang, C. Fan, H. Shen, Y. Chen, J. Dai, Biomimetic natural biopolymer - based wet - tissue adhesive for tough adhesion, seamless sealed, emergency/nonpressing hemostasis, and promoted wound healing, Adv. Funct. Mater. 33 (6) (2023) 2211340.

[19] K. Zhang, X. Chen, Y. Xue, J. Lin, X. Liang, J. Zhang, J. Zhang, G. Chen, C. Cai, J. Liu, Tough hydrogel bioadhesives for sutureless wound sealing, hemostasis and

biointerfaces, Adv. Funct. Mater. 32 (15) (2022) 2111465.

[20] Y. Liang, H. Xu, Q. Han, M. Xu, J. Zhang, J. Wang, X. Liu, Z. Yin, B. Guo, A Janus hydrogel sealant with instant wet adhesion and anti-swelling behavior for gastric perforation repair, Nano Today 54 (2024) 102105.

[21] P. Ma, W. Liang, R. Huang, B. Zheng, K. Feng, W. He, Z. Huang, H. Shen, H. Wang, D. Wu, Super - structured wet - adhesive hydrogel with ultralow swelling, ultrahigh burst pressure tolerance, and anti - postoperative adhesion properties for tissue adhesion, Adv. Mater. 36 (11) (2024) 2305400.

[22] G. Tian, D. Yang, C. Liang, Y. Liu, J. Chen, Q. Zhao, S. Tang, J. Huang, P. Xu, Z. Liu, D. Qi, A nonswelling hydrogel with regenerable high wet tissue adhesion for bioelectronics, Adv. Mater. 35 (18) (2023) 2212302.

[23] M. H. Ho, Q. v. Hilst, X. Cui, Y. Ramaswamy, T. Woodfield, J. Rnjak-Kovacina, S. G. Wise, K. S. Lim, From Adhesion to Detachment: Strategies to Design Tissue-Adhesive Hydrogels, Adv. Nanobiomed Res. 4 (2) (2024) 2300090.

[24] H. Y. Yuen, H. P. Bei, X. Zhao, Underwater and wet adhesion strategies for hydrogels in biomedical applications, Chem. Eng. J. 431 (2022) 133372.

[25] J. Yang, R. Bai, B. Chen, Z. Suo, Hydrogel adhesion: a supramolecular synergy of chemistry, topology, and mechanics, Adv. Funct. Mater. 30 (2) (2020) 1901693.

[26] Z. Xiao, Q. Li, H. Liu, Q. Zhao, Y. Niu, D. Zhao, Adhesion mechanism and application progress of hydrogels, Eur. Polym. J. 173 (2022) 111277.

[27] C. Heinritz, X. J. Ng, T. Scheibel, Bio - inspired protein - based and activatable adhesion systems, Adv. Funct. Mater. 34 (35) (2024) 2303609.

[28] Y. Ding, L. Yu, Z. Mao, Adhesion mechanisms and design strategies for bioadhesives, Colloid Interface Sci. Commun. 63 (2024) 100809.

[29] A. Štorha, E. A. Mun, V. V. Khutoryanskiy, Synthesis of thiolated and acrylated nanoparticles using thiol-ene click chemistry: towards novel mucoadhesive materials for drug delivery, RSC Adv. 3 (30) (2013) 12275-12279.

[30] T. T. H. Thi, Y. Lee, P. Le Thi, K. D. Park, Engineered horseradish peroxidase-catalyzed hydrogels with high tissue adhesiveness for biomedical applications, J. Ind. Eng. Chem. 78 (2019) 34-52.

[31] S. Tang, K. Feng, R. Yang, Y. Cheng, M. Chen, H. Zhang, N. Shi, Z. Wei, H. Ren, Y. Ma, Multifunctional Adhesive Hydrogels: From Design to Biomedical Applications, Advanced Healthcare Materials 14 (2) (2025) 2403734.

[32] A. S. Moghaddam, M. Bahrami, E. Sarikhani, R. Tutar, Y. N. Ertas, F. Tamimi, A. Hedayatnia, C. Jugie, H. Savoji, A. T. Qureshi, M. Rizwan, C. V. Maduka, N. Ashammakhi, Engineering the Immune Response to Biomaterials, Adv. Sci. 12 (19) (2025) 2414724.

[33] D. Gao, K. Parida, P. S. Lee, Emerging soft conductors for bioelectronic interfaces, Adv. Funct. Mater. 30 (29) (2020) 1907184.

[34] A. Roy, S. Zenker, S. Jain, R. Afshari, Y. Oz, Y. Zheng, N. Annabi, A highly stretchable, conductive, and transparent bioadhesive hydrogel as a flexible sensor for enhanced real-time human health monitoring, Adv. Mater. 36 (35) (2024) 2404225.

[35] S. Fuchs, K. Shariati, M. Ma, Specialty tough hydrogels and their biomedical applications, Adv. Healthc. Mater. 9 (2) (2020) 1901396.

[36] L. Vojtova, L. Michlovska, K. Valova, M. Zboncak, M. Trunec, K. Castkova, M. Krticka, V. Pavlinakova, P. Polacek, M. Dzurov, V. Lukasova, M. Rampichova, T. Suchy, R. Sedlacek, M.-P. Ginebra, E. B. Montufar, The effect of the thermosensitive biodegradable PLGA–PEG–PLGA copolymer on the rheological, structural and mechanical properties of thixotropic self-hardening tricalcium phosphate cement, Int. J. Mol. Sci. 20 (2) (2019) 391.

[37] X. Zhao, Q. Lang, L. Yildirimer, Z. Y. Lin, W. Cui, N. Annabi, K. W. Ng, M. R. Dokmeci, A. M. Ghaemmaghami, A. Khademhosseini, Photocrosslinkable gelatin hydrogel for epidermal tissue engineering, Adv. Healthc. Mater. 5 (1) (2016) 108-118.

[38] S. S. Liow, Q. Dou, D. Kai, A. A. Karim, K. Zhang, F. Xu, X. J. Loh, Thermogels: In situ gelling biomaterial, ACS Biomater.-Sci. Eng. 2 (3) (2016) 295-316.

[39] Q. T. Nguyen, Y. Hwang, A. C. Chen, S. Varghese, R. L. Sah, Cartilage-like mechanical properties of poly (ethylene glycol)-diacrylate hydrogels, Biomaterials 33 (28) (2012) 6682-6690.

[40] S. C. Tjong, Structural and mechanical properties of polymer nanocomposites, Mater. Sci. Eng. R Rep. 53 (3-4) (2006) 73-197.

[41] K. Y. Lee, J. A. Rowley, P. Eiselt, E. M. Moy, K. H. Bouhadir, D. J. Mooney, Controlling mechanical and swelling properties of alginate hydrogels independently by cross-linker type and cross-linking density, Macromolecules 33 (11) (2000) 4291-4294.

[42] P. Cao, L. Tao, J. Gong, T. Wang, Q. Wang, J. Ju, Y. Zhang, 4D printing of a sodium alginate hydrogel with step-wise shape deformation based on variation of crosslinking density, ACS Appl. Polym. Mater. 3 (12) (2021) 6167-6175.

[43] R. Wang, C. Cheng, H. Wang, D. Wang, Swollen hydrogel nanotechnology: Advanced applications of the rudimentary swelling properties of hydrogels, ChemPhysMater 3 (4) (2024) 357-375.

[44] H. Kamata, X. Li, U. i. Chung, T. Sakai, Design of hydrogels for biomedical applications, Adv. Healthc. Mater. 4 (16) (2015) 2360-2374.

[45] P. T. M. Albers, L. G. J. van der Ven, R. A. T. M. van Benthem, A. C. C. Esteves, G. de With, Water swelling behavior of poly (ethylene glycol)-based polyurethane networks, Macromolecules 53 (3) (2020) 862-874.

[46] M. Zhu, Y. Wang, G. Ferracci, J. Zheng, N.-J. Cho, B. H. Lee, Gelatin methacryloyl and its hydrogels with an exceptional degree of controllability and batch-to-batch consistency, Sci. Rep. 9 (2019) 6863.

[47] F. Della Sala, M. Biondi, D. Guarnieri, A. Borzacchiello, L. Ambrosio, L. Mayol, Mechanical behavior of bioactive poly (ethylene glycol) diacrylate matrices for biomedical application, J. Mech. Behav. Biomed. 110 (2020) 103885.

[48] S. Wang, J. Liu, L. Wang, H. Cai, Q. Wang, W. Wang, J. Shao, X. Dong, Underwater adhesion and anti-swelling hydrogels, Adv. Mater. Technol. 8 (6) (2023) 2201477.

[49] H. Yuan, T. Zhu, Y. Huang, Z. Wang, P. Han, L. Tan, J. Wu, X. Chen, P. Yao, C. Zhu, J. Xu, Hydrophobic and adhesive elastomer encapsulation for anti-drying, non-swelling, and adhesive hydrogels, Adv. Funct. Mater. 34 (51) (2024) 2409703.

[50] X. Jiang, X. Zhou, K. Ding, X. Li, B. Huang, W. Xu, Anti-Swelling Gel Wearable Sensor Based on Solvent Exchange Strategy for Underwater Communication, Adv. Funct. Mater. 34 (34) (2024) 2400936.

[51] W. Feng, Z. Wang, Tailoring the swelling-shrinkable behavior of hydrogels for biomedical applications, Adv. Sci. 10 (28) (2023) 2303326.

[52] W. Hu, Z. Wang, Y. Xiao, S. Zhang, J. Wang, Advances in crosslinking strategies of biomedical hydrogels, Biomater. Sci. 7 (2019) 843-855.

[53] Y. S. Zhang, A. Khademhosseini, Advances in engineering hydrogels, Sci. 356 (6337) (2017) eaaf3627.

[54] W. Gao, H. Ota, D. Kiriya, K. Takei, A. Javey, Flexible electronics toward wearable sensing, Acc. Chem. Res. 52 (3) (2019) 523-533.

[55] Z. Fan, J. C. Ho, T. Takahashi, R. Yerushalmi, K. Takei, A. C. Ford, Y. L. Chueh, A. Javey, Toward the development of printable nanowire electronics and sensors, Adv. Mater. 21 (37) (2009) 3730-3743.

[56] T. Daeneke, K. Khoshmanesh, N. Mahmood, I. A. De Castro, D. Esrafilzadeh, S. J. Barrow, M. D. Dickey, K. Kalantar-Zadeh, Liquid metals: fundamentals and applications in chemistry, Chem. Soc. Rev. 47 (11) (2018) 4073-4111.

[57] P. Tan, H. Wang, F. Xiao, X. Lu, W. Shang, X. Deng, H. Song, Z. Xu, J. Cao, T. Gan, B. Wang, X. Zhou, Solution-processable, soft, self-adhesive, and conductive polymer composites for soft electronics, Nat. Commun. 13 (1) (2022) 358.

[58] Q. Zhuang, K. Yao, C. Zhang, X. Song, J. Zhou, Y. Zhang, Q. Huang, Y. Zhou, X. Yu, Z. Zheng, Permeable, three-dimensional integrated electronic skins with stretchable hybrid liquid metal solders, Nat. Electron. 7 (7) (2024) 598-609.

[59] T. R. Ray, J. Choi, A. J. Bandodkar, S. Krishnan, P. Gutruf, L. Tian, R. Ghaffari, J. A. Rogers, Bio-integrated wearable systems: a comprehensive review, Chem. Rev. 119

(8) (2019) 5461-5533.

[60] S. Ganguly, S. Margel, Magnetic Ionogel and Its Applications, Gels 11 (4) (2025) 219.

[61] S. Pourshahrestani, E. Zeimaran, N. A. Kadri, N. Mutlu, A. R. Boccaccini, Polymeric hydrogel systems as emerging biomaterial platforms to enable hemostasis and wound healing, Adv. Healthc. Mater. 9 (20) (2020) 2000905.

[62] Y. Zhang, Y. Wang, Y. Li, Y. Yang, M. Jin, X. Lin, Z. Zhuang, K. Guo, T. Zhang, W. Tan, Application of collagen-based hydrogel in skin wound healing, Gels 9 (3) (2023) 185.

[63] B. Huang, D. Hu, A. Dong, J. Tian, W. Zhang, Highly antibacterial and adhesive hyaluronic acid hydrogel for wound repair, Biomacromolecules 23 (11) (2022) 4766-4777.

[64] Y. Xie, P. Gao, F. He, C. Zhang, Application of Alginate-Based Hydrogels in Hemostasis, Gels 8 (2) (2022) 109.

[65] J. Youn, K. D. Patel, A. W. Perriman, J.-S. Sung, M. Patel, L.-S. Bouchard, R. Patel, Tissue adhesives based on chitosan for biomedical applications, J. Mater. Chem. B 12 (41) (2024) 10446-10465.

[66] I. S. Bayer, Advances in fibrin-based materials in wound repair: a review, Molecules 27 (14) (2022) 4504.

[67] S. O. Sarrigiannidis, J. M. Rey, O. Dobre, C. González-García, M. J. Dalby, M. Salmeron-Sanchez, A tough act to follow: collagen hydrogel modifications to improve mechanical and growth factor loading capabilities, Mater. Today Bio 10 (2021) 100098.

[68] H. Yang, L. Song, Y. Zou, D. Sun, L. Wang, Z. Yu, J. Guo, Role of hyaluronic acids and potential as regenerative biomaterials in wound healing, ACS Appl. Bio Mater. 4 (1) (2020) 311-324.

[69] M. S. N. A. Azmir, M. N. Moni, A. Gobetti, G. Ramorino, K. Dey, Advances in modulating mechanical properties of gelatin-based hydrogel in tissue engineering, Int. J. Polym. Mater. 74 (3) (2025) 215-250.

[70] X. Gou, M. Zheng, Y. Zhao, X. Dong, F. Jin, J. Xing, X. Duan, Mechanical property

of PEG hydrogel and the 3D red blood cell microstructures fabricated by two-photon polymerization, Appl. Surf. Sci. 416 (2017) 273-280.

[71] M. A. Haq, Y. Su, D. Wang, Mechanical properties of PNIPAM based hydrogels: A review, Mater. Sci. Eng. C 70 (2017) 842-855.

[72] Y. Cao, X. Zhang, T. Xu, X. Zhang, L. Wang, Y. Wei, Z. Liang, H. Liu, L. Zhao, D. Huang, Mechanoactive wound dressing using poly (N-isopropyl acrylamide) based hydrogels, Eur. Polym. J. 202 (2024) 112645.

[73] W. Zhang, R. Wang, Z. Sun, X. Zhu, Q. Zhao, T. Zhang, A. Cholewinski, F. K. Yang, B. Zhao, R. Pinnaratip, P. K. Forooshani, B. P. Lee, Catechol-functionalized hydrogels: biomimetic design, adhesion mechanism, and biomedical applications, Chem. Soc. Rev. 49 (2) (2020) 433-464.

[74] Y. Yang, T. Xu, H. P. Bei, Y. Zhao, X. Zhao, Sculpting bio-inspired surface textures: an adhesive janus periosteum, Adv. Funct. Mater. 31 (37) (2021) 2104636.

[75] Y. Yang, D. Suo, T. Xu, S. Zhao, X. Xu, H.-P. Bei, K. K.-y. Wong, Q. Li, Z. Zheng, B. Li, X. Zhao, Sprayable biomimetic double mask with rapid autophasing and hierarchical programming for scarless wound healing, Sci. Adv. 10 (33) (2024) eado9479.

[76] S. Lyu, Q. Liu, H.-Y. Yuen, H. Xie, Y. Yang, K. W.-K. Yeung, C.-y. Tang, S. Wang, Y. Liu, B. Li, Y. He, X. Zhao, A differential-targeting core–shell microneedle patch with coordinated and prolonged release of mangiferin and MSC-derived exosomes for scarless skin regeneration, Mater. Horiz. 11 (11) (2024) 2667-2684.

[77] W. Li, Y. Dou, X. Li, S. Fang, J. Li, Q. Li, A highly effective, UV-curable, intumescent, flame-retardant coating containing phosphorus, nitrogen, and sulfur, based on thiol-ene click reaction, Materials 15 (9) (2022) 3358.

[78] D. S. Kazybayeva, G. S. Irmukhametova, V. V. Khutoryanskiy, Synthesis of hydrolytically and oxidation-responsive networks using thiol-ene "click" chemistry with pentaerythritol tetrakis (3-mercaptopropionate) and tri/tetra-acrylates, Polym. Adv. Technol. 32 (7) (2021) 2682-2689.

[79] X. Zhang, H. Nguyen, M. Daly, S. T. Nguyen, H. D. Espinosa, Nanoscale toughening of ultrathin graphene oxide-polymer composites: Mechanochemical insights into hydrogen-bonding/van der Waals interactions, polymer chain alignment, and steric parameters, Nanoscale 11 (25) (2019) 12305-12316.

[80] Y. Yang, Q. Zhang, T. Xu, H. Zhang, M. Zhang, L. Lu, Y. Hao, J. H. Fuh, X. Zhao, Photocrosslinkable nanocomposite ink for printing strong, biodegradable and bioactive bone graft, Biomaterials 263 (2020) 120378.

[81] X. Zhao, I. Olsen, H. Li, K. Gellynck, P. G. Buxton, J. C. Knowles, V. Salih, A. M. Young, Reactive calcium-phosphate-containing poly (ester-co-ether) methacrylate bone adhesives: chemical, mechanical and biological considerations, Acta Biomater. 6 (3) (2010) 845-855.

[82] G. Singh, A. Chanda, Mechanical properties of whole-body soft human tissues: a review, Biomed. Mater. 16 (6) (2021) 062004.

[83] A. Wahlsten, A. Stracuzzi, I. Lüchtefeld, G. Restivo, N. Lindenblatt, C. Giampietro, A. E. Ehret, E. Mazza, Multiscale mechanical analysis of the elastic modulus of skin, Acta Biomater. 170 (2023) 155-168.

[84] A. N. Annaidh, K. Bruyère, M. Destrade, M. D. Gilchrist, M. Otténio, Characterization of the anisotropic mechanical properties of excised human skin, J. Mech. Behav. Biomed. 5 (1) (2012) 139-148.

[85] S. J. M. Yazdi, J. Baqersad, Mechanical modeling and characterization of human skin: A review, J. Biomech. 130 (2022) 110864.

[86] A. Summerfield, F. Meurens, M. E. Ricklin, The immunology of the porcine skin and its value as a model for human skin, Mol. Immunol. 66 (1) (2015) 14-21.

[87] S. A. Ranamukhaarachchi, S. Lehnert, S. L. Ranamukhaarachchi, L. Sprenger, T. Schneider, I. Mansoor, K. Rai, U. O. Häfeli, B. Stoeber, A micromechanical comparison of human and porcine skin before and after preservation by freezing for medical device development, Sci. Rep. 6 (1) (2016) 32074.

[88] P. K. Whelton, R. M. Carey, G. Mancia, R. Kreutz, J. D. Bundy, B. Williams, Harmonization of the American College of Cardiology/American Heart Association

and European Society of Cardiology/European Society of Hypertension Blood Pressure/Hypertension Guidelines: Comparisons, Reflections, and Recommendations, Circulation 146 (11) (2022) 868-877.

[89] X. N. Zhang, Y. J. Wang, S. Sun, L. Hou, P. Wu, Z. L. Wu, Q. Zheng, A tough and stiff hydrogel with tunable water content and mechanical properties based on the synergistic effect of hydrogen bonding and hydrophobic interaction, Macromolecules 51 (20) (2018) 8136-8146.

[90] S. Nam, D. Mooney, Polymeric tissue adhesives, Chem. Rev. 121 (18) (2021) 11336-11384.

[91] Q. Huang, Z. Zheng, Pathway to developing permeable electronics, ACS Nano 16 (10) (2022) 15537-15544.

[92] Y. Yu, Y. Zheng, S. Sun, X. Wu, Z. Wang, Decoupling volume shrinkage from dehydration in hydrogels via hierarchical structural design for sustained cushioning and humidity regulation, Chem. Eng. J. 529 (2026) 173237.

[93] G. Ghosh, A. Bag, A. Hanif, M. Meeseepong, Y. R. Lee, N. E. Lee, Tough, bio-disintegrable and stretchable substrate reinforced with nanofibers for transient wearable electronics, Adv. Funct. Mater. 33 (9) (2023) 2209277.

[94] K. Choi, S. Nam, Y. Lee, M. Lee, J. Jang, S. J. Kim, Y. J. Jeong, H. Kim, S. Bae, J.-B. Yoo, S. M. Cho, J.-B. Choi, H. K. Chung, J.-H. Ahn, C. E. Park, B. H. Hong, Reduced water vapor transmission rate of graphene gas barrier films for flexible organic field-effect transistors, ACS Nano 9 (6) (2015) 5818-5824.

[95] J. L. Down, A literature review of cyanoacrylate adhesives, Stud. Conserv. 46 (sup1) (2001) 35-38.

[96] A. Athavale, M. Thao, V. S. Sassaki, M. Lewis, V. Chandra, E. Fukaya, Cyanoacrylate glue reactions: a systematic review, cases, and proposed mechanisms, J. Vasc. Surg. Venous Lymphat. Disord. 11 (4) (2023) 876-888. e871.